Cenozoic Structural Deformation and Mechanisms of Exhumation of the Metamorphic Complexes in Southeastern Tibetan Plateau: Implications for Intraplate Middle-lower Crustal Flow in Response to Continental Collision

Xiaoyu Chen[1]*, Jean-Pierre Burg[2], Junlai Liu[1]*, Jiaxin Yan[1], Wenkui Fan[1], and Chunqiang, Zhao[1]

[1]State Key Laboratory of Geological Processes and Mineral Resources, China University of Geosciences, Beijing 100083, China

[2] Department of Earth Sciences, ETH Zurich, Sonneggstrasse 5, 8092, Zurich, Switzerland

Corresponding author: xiaoyu Chen (xiaoyuchen@cugb.edu.cn) ; Junlai Liu (jliu@cugb.edu.cn)

Key Points:

- Dome structures with high-grade metamorphic cores are widely developed in the southeastern Tibetan Plateau.
- Metamorphic cores of the domes were exhumed through two-stage cooling that initiated diachronously from ca. 30 Ma.
- Formation and exhumation of the domes are ascribed to middle and lower crustal flow in response to the India-Eurasia collision.

Abstract

Responses to the India-Eurasia plate collision vary significantly in different regions. In Southeastern Tibetan Plateau, the tectonic extrusion of the Sundaland block accommodated the tectonic convergence between the two plates. However, there have been extensive controversies over the mechanism of extrusion of the block. In this study, we focus on macro- and micro-scopic structural analysis, kinematics, timing of shearing and thermal histories of several typical metamorphic complexes in order to understand the tectonic processes driving the deformation of the complexes and extrusion of the block. It is shown that dome structures cored by the metamorphic rocks are widely developed in Southeast Tibetan Plateau. The cores are composed of high-grade metamorphic and high temperature deformed rocks, while the mantle parts are characterized by low-grade metamorphic rocks and low temperature deformation. Thermochronological data reveal that most of the domes began to be exhumed since 30 Ma, while the initiation of doming was diachronous at different places and mostly through two-stage cooling histories. In most of the domes, shear discontinuities exist between the core and mantle parts. We show that the formation and exhumation of the dome structures are related to subhorizontal middle and lower crustal flow, during which shearing, folding and exhumation are simultaneous. The middle and lower crustal flow resulted in lateral crustal flow and vertical exhumation of crustal masses, which absorbed a large amount of deformation of the lateral escape of Sundaland block during India-Eurasia collision.

Key words: Domes, Middle-lower crustal flow, Exhumation, Southeastern Tibetan Plateau

1 Introduction

The India-Eurasia plate collision and subsequent post-collisional processes since ca. 55 Ma have important influences on the formation and evolution of crustal structures in Tibetan Plateau, Southeastern Tibet Plateau, and in Southeast Asia (Molnar & Tapponnier, 1975; Morley, 2002). Responses to the India-Eurasia plate collision vary significantly in different regions. Alternative vertical and lateral extrusion of crustal masses occurred from the Himalaya to southeastern Tibet in accommodation of the tectonic convergence of the plates, i.e., 1) crustal thickening and mass vertical extrusion in the Himalayas by thrusting at ca. 55-45 Ma, 2) extensional collapse of the orogenic belt at ca. 41–30 Ma within and near the Ailao Shan–Red River belt in Southeastern Tibetan Plateau, 3) lateral extrusion of the Sundaland block accommodated by middle- to lower-crustal ductile flow possibly from 36 Ma within the block and shearing at ca. 28–20 Ma along the Ailao Shan–Red River belt, and 4) vertical mass extrusion by major faulting along the Main Central thrust and South Tibet detachment system in the High Himalaya since ca. 23 Ma (Liu et al., 2020 and references therein).

Various models were proposed to explore how the lithosphere accommodated the tectonic extrusion of the Sundaland block in Southeastern Tibetan Plateau. However, there have been extensive controversies over the mechanism of extrusion of the block. Most previous works (e.g., Briais et al., 1993; Leloup et al., 1993, 1995, 2001; Peltzer & Tapponnier, 1988; Tapponnier et al., 1990) were carried out based on the classical tectonic escape model proposed by Tapponnier et al. (1982). The model assumed that the Indian plate acted as a rigid indentor into the softer, wider Eurasian margin. Consequently, the Sundaland (Indochina) block extruded southeastward out of the plateau. The model emphasized the existence of a rigid lithospheric block. Main deformation during the extrusion is localized along the margins of the block. Strike-slip faults that cut through the whole lithosphere have large displacements with high rates (Armijo et al., 1989; Peltzer & Tapponnier, 1988; Tapponnier et al., 1986, 1990). Therefore, tectonic extrusion during convergence of the India-Eurasia continental plates was mainly accomplished by large-scale strike-slip faulting. However, crustal flow model stressed on the existence of a viscous mid- and lower crust in the Tibetan Plateau (Royden et al., 1997). Orogenic thickening in the plateau resulted in gravitational loading that forced the weak mid- and lower crust flowing out of the plateau. Magnetotelluric (MT) imaging (Bai et al., 2010) and seismic studies (Liu et al., 2014) provided arguments for the existence of such a low-viscosity lower crust underneath the plateau and along the southeastern margin of the plateau (Bai et al., 2010; Nelson et al., 1996; Rippe & Unsworth, 2010). The continental crust was deformed through regional flow along the weak mid- to lower- crustal material over 1000 km distances beyond the Eastern Himalayan syntaxis (Clark & Royden, 2000). Channel flow of low-viscosity middle to lower crust has been applied to interpret the outward growth of the Tibetan plateau (Beaumont et al., 2001; Clark & Royden, 2000; Royden et al., 1997; Shen et al., 2001), and the magnitude of dynamic topography at the eastern and southeastern Plateau margins (Clark et al., 2005). As an example, the 2008 Wenchuan earthquake was considered as resulting from faulting triggered and driven by eastward flowing of the Tibetan lower crust (Burchfiel et al., 2008).

In the Sundaland block, there exist several metamorphic complexes with Precambrian basement, most of which are distributed along the ductile high strain zones, e.g., Xuelong Shan, Diancang Shan, Ailao Shan, Yao Shan and Day Nui Con Voi (DNCV) complexes along the Ailao Shan-Red River (ASRR) tectonic belt, the Chongshan complex along the Chongshan tectonic belt, and the Gaoligong and Mogok complexes along the Gaoligong-Sagaing (GLG-SG) tectonic belt (Figure 1, Chen et al., 2016; Leloup et al., 1995). However, some metamorphic

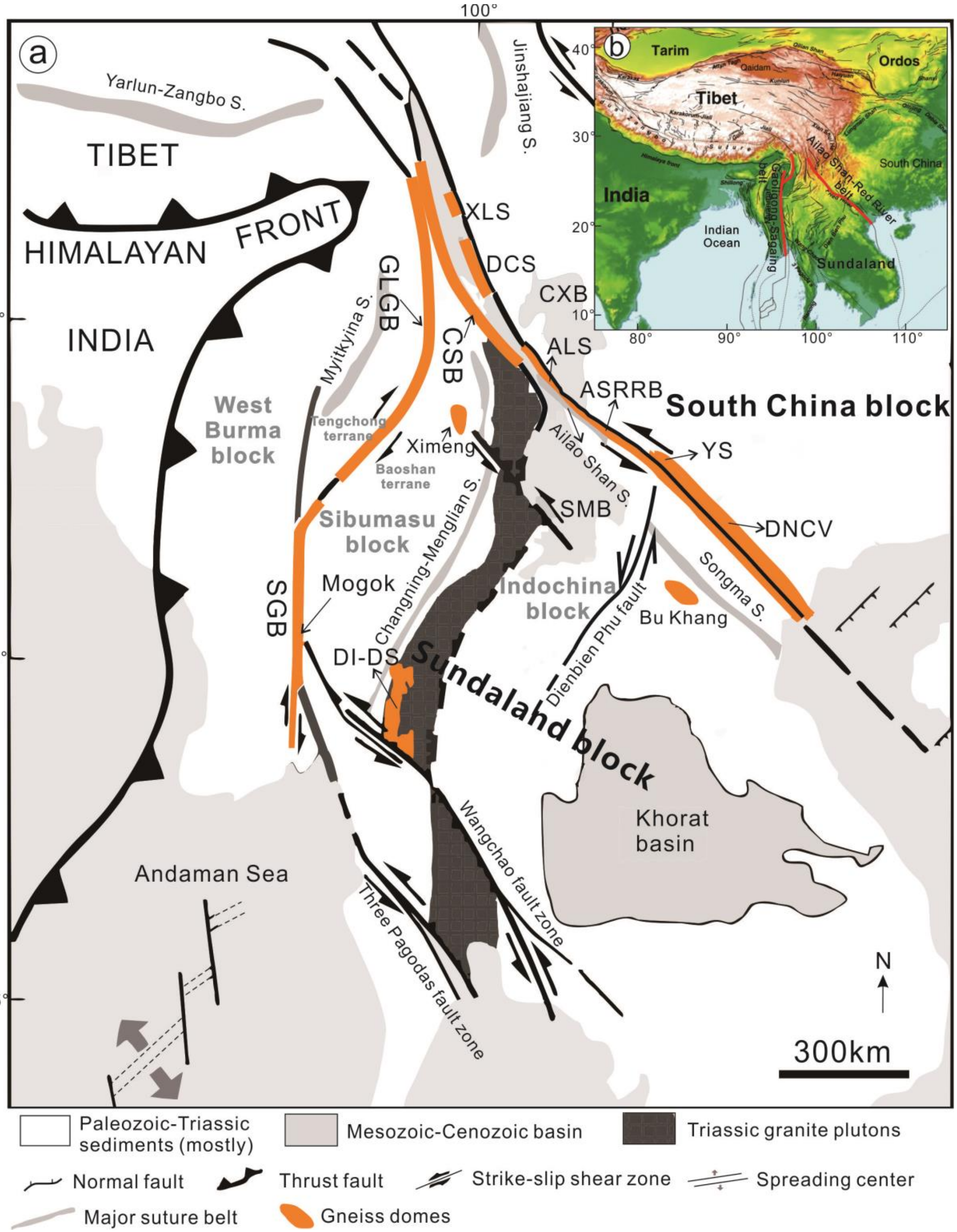

Figure 1. (a) Tectonic map showing the major tectonic belts and domains in Southeast Tibet plateau (Modified after Leloup et al., 1995). (b) Tectonic map of the India-Eurasia collision. ALS: Ailao Shan complex; ASRRB: Ailao Shan-Red River tectonic belt; CSB: Chong Shan tectonic belt; CXB: Chuxiong basin; DCS: Diancang Shan complex; DNCV: Day Nui Con Voi complex; DI-DS: Doi Inthanon-Doi Suthep

complex; GLGB: Gaoligong tectonic belt; S.: Suture zone; SMB: Simao basin; SGB: Sagaing tectonic belt; XLS: Xuelong Shan complex; YS: Yao Shan complex.

complexes, e.g., Ximeng and Bukang complexes, are in the interior of the block between the high strain zones (Figure 1, Chen et al., 2017a; Jolivet et al., 1999). Their existence provides new clues to elucidate the Cenozoic crustal deformation in Southeastern Tibet and Southeast Asia. In this paper, we focus on macro- and micro-scopic structural analysis, kinematics, timing of shearing and thermal histories of several typical metamorphic complexes, in order to define their structural configuration, exhumation process and timing, and to discuss the lateral escape mechanism of the Sundaland block. A new geodynamic model of middle-lower crustal flow in Southeastern Tibetan plateau is suggested on such a basis.

2 Tectonic Setting

2.1 The Sanjiang-SE Asia Tethys tectonic domain

The Sanjiang-SE Asia Tethys tectonic domain in Southeastern Tibetan plateau is distributed in a fan-shaped area converging to the eastern syntaxis. The domain is separated from the South China block to the east by the ASRR tectonic belt and from the west Burma block to the west by the GLG-SG tectonic belt (Figure 1). The tectonic framework of the domain is the result of superimposition of Tethyan tectonics by Cenozoic deformation. The former was formed by amalgamation of several micro-continents, e.g., western Burma, Sibumasu and Indochina blocks, which were separated by major or subsidiary Tethyan suture or rift zones, e.g., Changning-Menglian suture zone, Jinshajiang-Ailao Shan-Song Ma suture zone and Ganzi-Litang-Song Da rift zone (Figure 1, Chen et al., 2019). Tectonic studies suggest that these blocks were split from the northern margin of Gondwana continent, drifted northward and amalgamated to the southern margin of Eurasian continent successively since Late Paleozoic (Feng et al., 2005; Metcalfe, 1996).

The Changning-Menglian suture zone is the relics of the main Tethyan oceanic basin that opened in Early Devonian-Permian, and closed in Early-Middle Triassic (Metcalfe, 1996). To the west of the suture zone is the Sibumasu block with Gondwana affinity, and to the east is the Indochina block and the South China block. During the subduction of the Changning-Menglian oceanic plate, Permo-Triassic Lincang-Sukhothai magmatic arc was developed which is located on the eastern side of the ophiolite belt due to eastward subduction (Jian et al., 2009).

In addition, an important suture zone, i.e., the Jinshajiang-Ailao Shan-Song Ma suture zone, was developed in the Tethys tectonic domain (Figure 1). As a subsidiary Tethys ocean basin, the Jinshajiang-Ailao Shan-Song Ma ocean opened no later than Early Carboniferous and closed before Middle-Late Triassic during the convergence of Indochina block and South China plate (Metcalfe, 2013; Wu et al., 2016). Westward subduction of the Jinshajiang-Ailao Shan-Song Ma oceanic plate since Early Permian resulted in intraplate extension and rifting of the passive continental margin of South China plate, forming the Ganzi-Litang-Song Da rift zone to the east of the Jinshajiang-Ailao Shan-Song Ma suture zone (Wu et al., 2016).

The main part of the Indochina block covered by a set of Mesozoic-Cenozoic strata, is located between the Changning-Menglian suture zone and the Ailao Shan-Red River tectonic belt (Figure 1). The main body of the block is the Lanping - Simao Basin in China, and the Khorat Basin in Thailand. Cambrian strata are mainly exposed in the Wuliangshan area and have undergone intense deformation and metamorphism. Carboniferous-Permian strata are a set of volcanic-sedimentary rocks in the central and southern part of the block. Middle Triassic is mainly developed in the Xiaohejiang area between Jinggu and Simao area, which are mainly composed of carbonate, clastic rocks and turbidite. Upper Triassic is a set of clastic rocks, marl, and conglomerate rocks. Marine sedimentation continued to middle Jurassic (clastic and carbonate rocks), and turned into terrestrial sedimentation after Late Jurassic. A set of fluvial and lacustrine red clastic rocks, i.e., red beds, gypsum layers, salt layers and coal, were deposited as a result.

The Sibumasu block is composed of Tengchong and Bao Shan terranes in China (Figure 1). The block is separated from the West Burma block to the west by the GLG-SG belt and the Indochina block to the east by the Changning-Menglian suture zone. The block possesses Precambrian crystalline basement (Zhang et al., 2017), and a set of sedimentary association of Paleozoic terrestrial clastic rocks and shallow-marine carbonate, and Mesozoic terrestrial sedimentary strata (Bender, 1983). In the Late Carboniferous-Early Permian, glacial-marine sediments, cold water fauna and Gondwana flora are preserved, suggesting their Gondwana affinity.

2.2 Cenozoic tectonic framework

The Southeastern Tibetan plateau is characterized by three prominent ductile high strain zones (Figure 1, Leloup et al., 1995). These are, from west to east, the GLG-SG, Chongshan and ASRR tectonic belts (Figure 1), which superimposed, reactivated, or transformed the Tethys tectonic units. The three shear belts converge near the eastern Himalayan syntaxis, and diverge southward, depicting the structural framework and topography of Sanjiang-SE Asia. Traditionally, it was believed that the left lateral strike-slip displacement along the ASRR belt and the right lateral strike-slip displacement along the GLG-SG belt adjusted the lateral escape of Sundaland block (Tapponnier et al., 1986, 1990). However, ductile shear structures are also distributed outside the high-strained shear belts, e.g., the Ximeng and the Bukhang complexes within the Sundaland block (Chen et al., 2017a; Jolivet., 1999). Some authors also proposed dome model of the complexes along the shear belts (Anczkiewicz et al., 2007; Jolivet et al., 1999, 2001), questioning the nature of strike-slip shearing along these shear belts.

The Ailao Shan-Red River tectonic belt separates the South China block and Sundaland block in Southeastern Tibet Plateau (Figure 1). This belt is thought to form the northeast boundary of the extruded Sundaland block. The high strain zone extends over 1000 km from eastern Himalayan syntaxis to the South China Sea (Leloup et al., 1995). Four elongated metamorphic complexes were exposed along this belt, i.e., Xuelong Shan, Diancang Shan, Ailao Shan, Yao Shan-Day Nui Con Voi from north to south (Figure 1, Leloup et al., 1995). The metamorphic complexes are composed of highly sheared rocks that bear key information about the evolution of high strain zone, showing strongly developed foliation and lineation structures, A-type folds, widely developed mylonites, etc. Mylonitic foliations generally strike NW-SE, and stretching lineations are subparallel. A sequence of calc-alkaline and high-potassium alkaline magmatic rocks (Liang et al., 2007) are distributed along and near the belt. The ductile shear belt was cut by dextral strike-slip Red River fault with normal component on the northeastern margin since ca. 5 Ma (Tapponnier et al., 1986).

The Gaoligong-Sagaing tectonic belt, ~600 km in length, extends N-S from the eastern Himalayan syntaxis to the Longling-Ruili area, and to the south bends to the northeast to link with the Sagaing fault (Figure 1, Morley, 2007). The belt is considered as the western boundary of the Sundaland block. Dextral ductile shear sense indicators are widely preserved along the belt (Tapponnier et al., 1982). This zone can be further divided into granitoid and high-grade gneiss units (Zhang et al., 2012). The granitoid unit in the western part of the belt was resulted from the northward subduction of the Neotethyan slab (Lee et al., 2003; Zhang et al., 2012). The high-grade gneiss unit (i.e., the Gaoligong Group) has long been described as the Precambrian basement that experienced high-grade metamorphism (BGMRYP, 1990). The gneisses experienced highly ductile shearing forming mylonite belt.

The Chongshan tectonic belt lies between the Sibumasu block and Lanping-Simao basin (Figure 1). The belt extends generally along the Biluoxueshan and Chongshan mountains and the Lancang River, and connects with the Lincang granite belt southeastward (Zhang et al., 2010). The northern section of the belt strikes roughly N-S, parallel to the Gaoligong tectonic belt. The middle and southern section strikes NW-SE, with a length of more than 500 km and a width of 2-20 km. The east side of the belt is bounded by the Lancangjiang fault zone, adjacent to the Indochina block, while the west side of the belt is adjacent to the Baoshan terrane. The Proterozoic Chongshan group are exposed in the main part of the Chongshan tectonic belt, and the Mesozoic low-grade metamorphic rocks are mainly on both sides. These rocks experienced highly sheared.

North and south of the ASRR tectonic belt, the Chuxiong and Lanping-Simao basins are folded by NW to NNW trending anticlines, implying NE to ENE directed shortening compatible with left-lateral shearing along the ASRR tectonic belt (Lacassin et al., 1996; Leloup et al., 1995).

3 Major Cenozoic metamorphic complexes in SE Tibet and SE Asia

3.1 The Diancang Shan complex

The Diancang Shan complex, striking NW-SE, is in the northern part of the ASRR tectonic belt (Figure 1). Surface exposure pattern exhibits an elliptic shape with a length of about 80 km and a width of 12~20 km (Figure 2). It is separated from the Ailao Shan complex to the south by the Midu gap (Figure 1, Leloup et al., 1995). The core part of the complex is mainly composed of high-grade metamorphic rocks in the west, the superposed retrogressive metamorphic belt in the east, and granitic intrusions of various ages (Figure 2, Cao et al., 2011a, b). The complex is mantled by low-grade metamorphic Mesozoic strata belonging to the Lanping basin to the south and west, and is separated from the weakly metamorphic Paleozoic strata to the east by Quaternary normal faults (Figure 2).

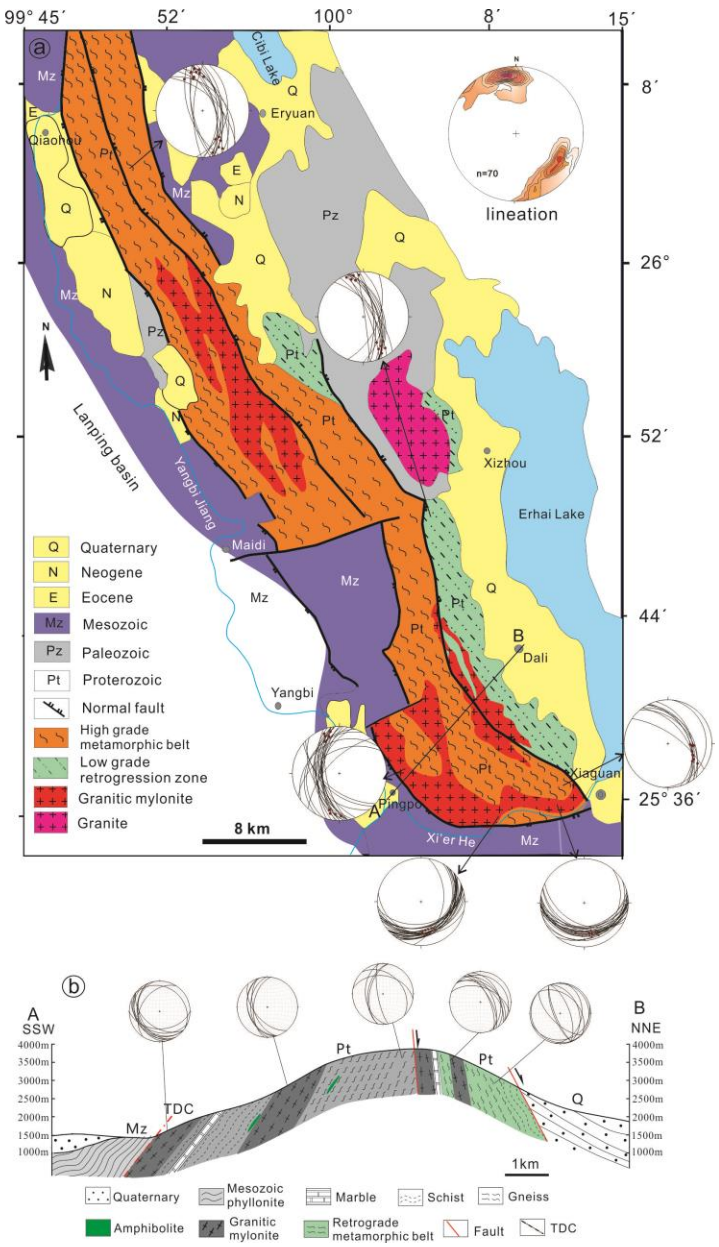

Figure 2. (a) Geological map of the Diancang Shan complex with stereographic projections of foliations and lineations (Modified after Cao et al., 2011a); (b) Geological section across the complex. TDC: Shear discontinuity.

The high-grade metamorphic rocks, with protolith ages of Paleoproterozoic to Mesoproterozoic (Cao et al., 2011a), include amphibolites, sillimanite garnet biotite gneisses, garnet biotite schists, biotite schists, marbles, etc., up to upper amphibolite facies (Figure 3a-f). The rocks were generally subjected to Cenozoic ductile shear deformation, resulting in the development of a set of typical L>>S, L, L-S tectonic rocks (Cao et al., 2010, 2011a, b). Granitic rocks are widespread in the core part, especially in the southern part of the complex. They are ascribed to three major tectono-magmatic events according to the published geochronology data, i.e., Neoproterozoic, Early-Middle Triassic and Cenozoic (Cao et al., 2011a; Chen et al., 2019). Most granitic rocks were subjected to various degrees of ductile shear deformation, forming a sequence of granitic mylonites (Figure 3a).

The superposed retrogressive metamorphic belt is located along the eastern flank of the complex and cut by normal faults along its eastern margin (Figure 2). Different from the high-grade metamorphic rocks, rocks in this belt are characterized by extensive retrograde metamorphism and normal-slip brittle-ductile deformation. Greenschist facies retrograde metamorphism was superimposed on early amphibolite facies metamorphic rocks. Chloritized schists and phyllites are the results of the retrograde metamorphism during deformation at shallow level during a late-stage deformation (Cao et al., 2011b). Mineral assemblages, e.g., sericite, chlorite, and other newly-born metamorphic minerals, of lower greenschist facies were developed in the retrograde metamorphic belt.

Rocks forming in the low-grade mantle at the southern and western parts, e.g., schists, phyllites, marbles, etc., were also subjected to ductile shearing. Quartz veins in the schists were sheared into boudinages indicating top-to-the SE shearing (Figure 3g). Laminated structures are common in the sheared marbles (Figure 3h).

Statistical analysis reveals that the Diancang Shan is a destructed A-type dome which is cored by the Paleoproterozoic to Mesoproterozoic high-grade metamorphic rocks and mantled by Paleozoic-Mesozoic low-grade metamorphic rocks. In the northern section, the overall foliations strike NNW-SSE, and sub-horizontal stretching lineations slightly plunge NNW or SSE. The foliations mainly dips to SW (Figure 2), with dominant left-lateral shear indicators, indicating top-to-the SE kinematics, i.e., the high-grade metamorphic rocks in the core moved northwestward in relation to the low-grade metamorphic rocks in the mantle. However, the foliations dip southeast or south at the southern flank. Top-to-the southeast kinematics indicate that the high-grade metamorphic rocks in the lower plate were sheared NW-ward in relation to the Triassic low-grade metamorphic rocks in the upper plate (Figures 3a-3c). The parallelism of the long axis of the elongated configuration of the dome with stretching lineation and hinges of widespread outcrop-scale A-type folds (Figure 3d) suggests that the Diancang Shan is a destructed monoclinal A-type fold. The east limb of the dome was truncated by Holocene normal faults in the north segment.

$^{40}Ar/^{39}Ar$ dating of hornblende, muscovite, biotite, and K-feldspar minerals from the mylonites in the core part yielded ages of 27–23 Ma, 23–13 Ma, 11.67–6.44 Ma and 9-4 Ma, respectively (Cao et al., 2011b). Cooling paths derived from these data show that there are two stages of dominant cooling and exhumation. The first stage started diachronously northward from >27 to 23 Ma, with relatively slow exhumation rates (cooling rate of 11-21°C/Ma) until ca. 13 Ma. The late stage is diachronous and with relatively fast cooling rates of 45-50°C/Ma throughout the whole period from 13 to 0 Ma.

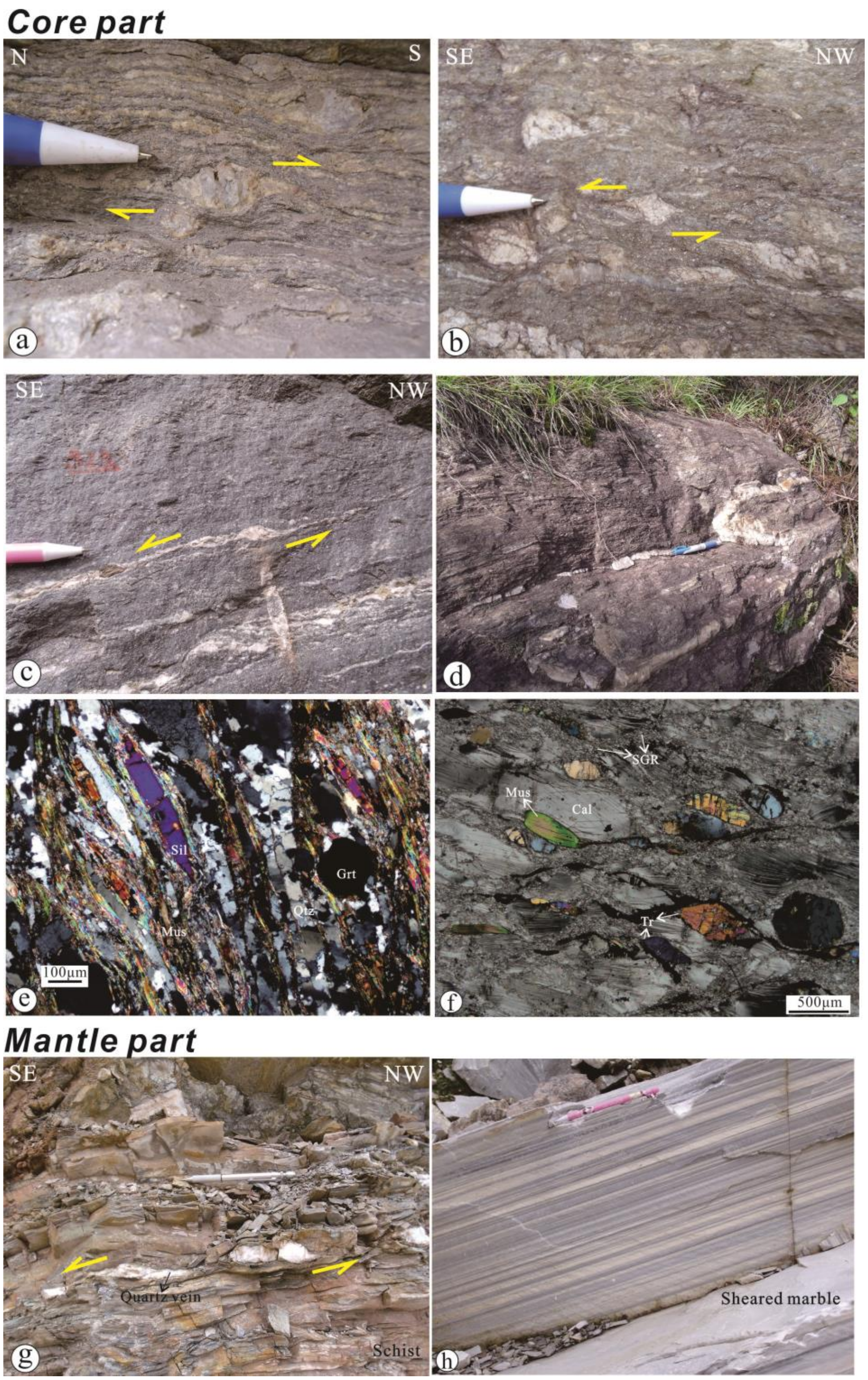

Figure 3. Macro- and micro- structures of the rocks from the core and mantle parts of the Diancang Shan complex. a: Granitic mylonite from the southern slope with K-feldspar porphyroclasts indicating top-to-the S shearing; b: Felsic layers in the migmatic gneiss were sheared into lenses indicating top-to-the SE shearing; c: Felsic dykes were sheared into stair-step indicating top-to-the SE shearing; d: A type fold developed in the

biotite quartz schist e: Oriented sillimanite, muscovite, and quartz aggregate in the sillimanite garnet two mica schist. Quartz grains show grain boundary migration; f: The calcite grains experienced subgrain rotational recrystallization, tremolites are as porphyroclasts, muscovite grains are sheared into mica fishes in tremolite marble; g: The quartz vein in the Triassic phyllite was sheared into lens, and its trailing direction indicates top-to-the SE shearing; h: The Triassic marble was sheared into laminated structure. SGR: Subgrain rotational recrystallization.

3.2 The Ailao Shan complex

The Ailao Shan complex is the most significant complex along the ASRR tectonic belt, trending NW-SE for about 400 kilometers long (Figure 1) from the Nanjian county southward to northwestern Vietnam. The Vietnamese part of the Ailao Shan massif, i.e., the Fansipan complex, is mainly composed of granitic gneisses and granites with minor pieces of metasediments (Anczkiewicz et al., 2007). The Ailao Shan complex is mainly composed of two belts, i.e., the high-grade metamorphic belt in the east and the low-grade metamorphic belt in the west (Figure 4). The high-grade metamorphic belt is mainly composed of Paleoproterozoic Ailao Shan group and intrusions of various age. The high-grade belt is cut by the Ailao Shan fault to the west and the Red River fault to the east (Figure 4). Rocks in the high-grade belt underwent multi-stage ductile deformation at high temperature of up to upper amphibolite to granulite facies. Extensive partial melting gave rise to various type of migmatites (Leloup et al., 1993, 1995; Wu et al., 2016). The low-grade metamorphic belt to the west of the Ailao Shan fault is cut by the Jiujia-Anding fault further west (Figure 4). The belt is mainly composed of Paleozoic-Mesozoic greenschist facies metamorphic rocks, which also suffered from ductile shearing at relative low temperatures (Wu et al., 2016).

Two typical cross-sections from the northern and middle segments of the Ailao Shan complex (Figure 4) are chosen to show the macroscopic structural style and microstructural variations.

3.2.1 The Shujie section

The Shujie profile across the northernmost end of the Ailao Shan complex (Figures 4a and 4b), has a total length of ca. 7 km. The high-grade metamorphic belt dies out northward near the section. The overall structural configuration of the Ailao Shan complex at the northern end form an antiformal structural pattern. High-grade gneisses of Proterozoic protoliths in the core are mantled by low-grade meta-sedimentary rocks of Late Paleozoic to Mesozoic. The latter transits into sedimentary rocks in the Chuxiong and Simao basins on both sides of the complex (Figure 4b). In the high-grade metamorphic core, there are schists, gneisses, migmatites and granitic intrusions. Mylonization is strongly developed due to Cenozoic ductile shearing. The Permian low-grade metamorphic zone comprises metamorphic siltstones, marbles, slates, phyllites and schists, etc., which were also experienced ductile shearing at low temperature.

Structural reconstruction using foliation attitudes along the whole section (Figure 4b) characterizes a normal anticlinal structure. Foliations in the southwestern limb dip SE. Sinistral shear sense indicators are consistent with top to SE shearing. Along the northeastern limb, foliations dip NE with mostly dextral shear senses, also indicating top to SE shearing. From the core part to the two limbs, the deformation temperature gradually decreases. However, the lineations from the core and two limbs are stable, plunging NW or SE. The consistency in the orientation of lineations and kinematics imply that both high-grade and low-grade metamorphic rocks experienced concurrent ductile shearing, and the differences in deformation microstructures and metamorphic associations are possibly resulted from variations in structural horizons in the crust.

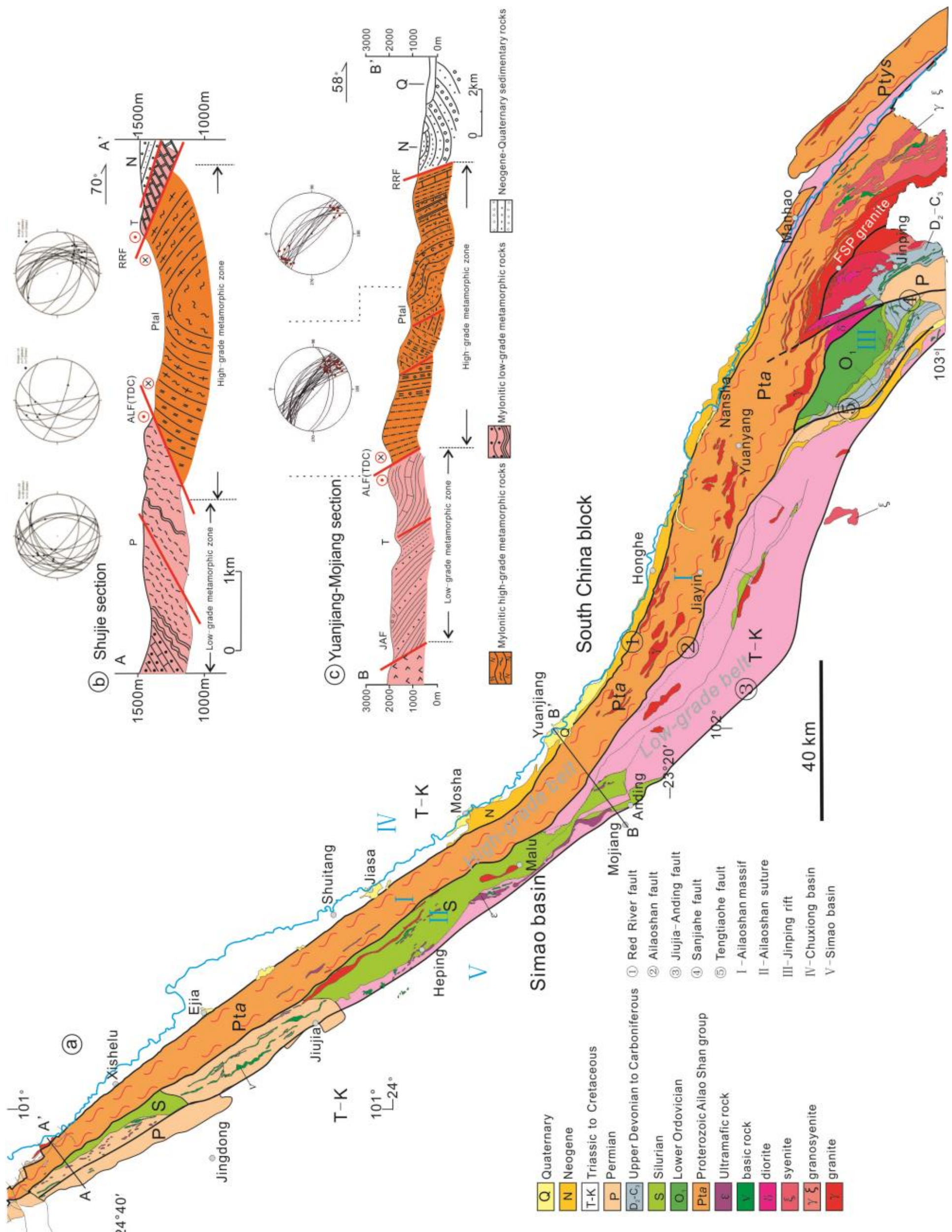

Figure 4. (a) Geological map of the Ailao Shan complex. (b-c) Geological sections across the complex. The Shujie section in the northern part (b), and the Yuanjiang-Mojiang section in the middle part (c).

3.2.2 The Yuanjiang-Mojiang section

The Yuanjiang-Mojiang profile is in the middle part of the Ailao Shan complex, with a total length of about 40 km (Figure 4). Two metamorphic belts that have identical structural geometry but contrasting metamorphic grades are distributed along the section. At the northeastern part, a high-grade metamorphic zone mainly consists of gneisses, marbles, amphibolites, and schists. Granitic mylonites, weakly deformed, or undeformed granites are also exposed in the high-grade zone. The Triassic low-grade metamorphic belt to the west of the high-grade belt mainly contains phyllites, slates, crystalline limestones, and metamorphic sandstones, which also show evidence of ductile shearing.

The foliations and lineations of the whole section show remarkable consistency. Mylonitic foliations overall strike NW-SE, dip to NE with large dip angles, or are sometimes subvertical (Figs. 4c and 5a, b). The lineations plunge consistently NW or SE, with small plunging angles (Figure 4c). The foliations are locally folded with fold hinges parallel to the local lineations, forming A-type folds (Figure 5c). Migmatization is strongly developed in the gneisses in the high-grade metamorphic belt. Leucocratic layers are interbedded with mica-rich layers. Feldspar grains were locally sheared into porphyrpclasts (Figures 5d and 5e), indicating top-to-the NW shearing, i.e., the high-grade metamorphic rocks move NW relative to the low-grade metamorphic rocks. Leucogranite dykes are concordant with the foliations (Figure 5f), or sheared into tectonic lenses, or cross-cut the mylonitic foliations (Figure 5g). Some of the felsic veins were folded into small-scale folds during progressive shearing. In such cases, the hinge zones of the folds are thickened or thinned owing to progressive shearing (Figure 5h).

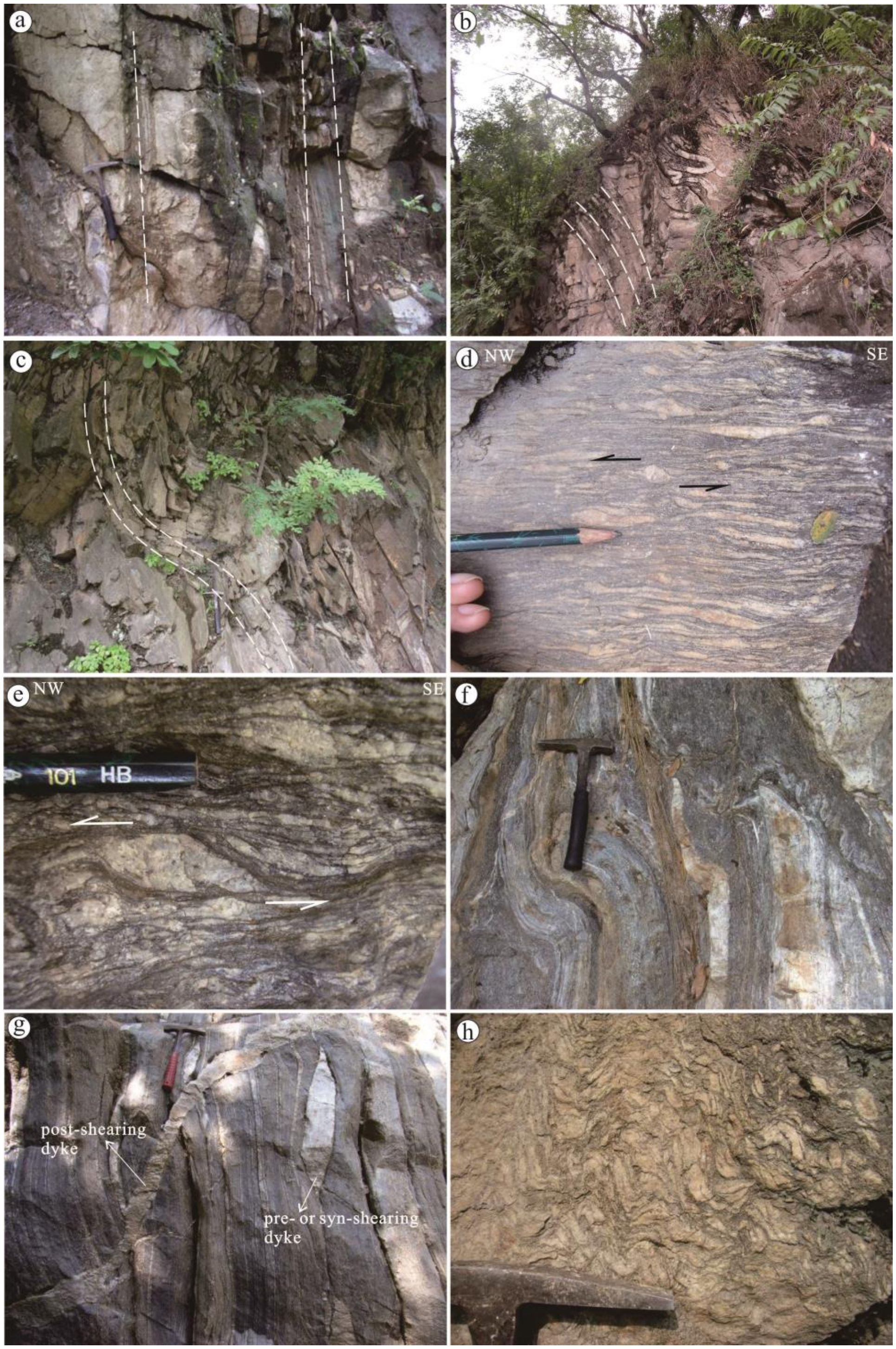

Figure 5. Macrostructures of the Yuanjiang-Mojiang section. a and b: The nearly vertical foliation developed in the granitic mylonite. c: Foliations were locally folded. d and e: In biotite quartz schist, the rocks were differentiated, the feldspar layers are interbedded with the mica enriched layers, the felsic layers were sheared into lenses shape, σ porphyroclasts, indicating top-to-the NW shearing. f: Migmatic biotite plagioclase gneiss, the felsic veins developed along the foliations. g: Leucogranite dykes were sheared into tectonic lenses

concordant with the foliations, or cross-cut the mylonitic foliations. h: The felsic veins were folded into small-scale folds during progressive shearing, the hinge zones of the folds are thickened or thinned owing to progressive shearing.

Comprehensive structural analyses of the whole section, high-grade metamorphic rocks of up to high amphibolite facies are exposed in the east segment, including forsterite bearing marbles, gneisses, etc. (Figures 6a-6c). In the hornblende biotite plagioclase gneisses, the amphibole and biotite grains do not show obvious intragranular plastic deformation, but are strongly oriented (Figure 6b). Granitic rocks mostly possess gneissic structures, without evidence for grain sizes reduction (Figure 6c), which may reflect high temperature recovery during Cenozoic shearing. In the middle-western part of the profile, rocks experienced intensive high-temperature mylonitization. Myrmekite are obviously developed along the rims of K-feldspar grains in the high-temperature granitic mylonite (Figure 6d), as the result of precipitation of quartz between plagioclase and K-feldspar grains due to metasomatism. Rectangular polycrystalline bands of quartz grains form the foliations, reflecting the dominance of high-temperature static recovery (Figure 6e). In such tectonites, feldspar grains are usually in the form of porphyroclasts (Figures 6d and 6e). These deformation microstructures are indicative of deformation temperature at about 550-650℃ (Passchier and Trouw, 2005). Medium-temperature mylonites are distributed along the eastern side of the Ailao Shan fault. The rocks are characterized by intensive grain size reduction (Figure 6f). Quartz grains were deformed by early stretching into quartz ribbons, then by subsequent subgrain rotation recrystallization during progressive shearing (Figure 6f). The microstructures are compatible with deformation temperatures of approximately 450-550℃ (Passchier and Trouw, 2005). There is mainly a sequence of phyllonites in the sheared Triassic rocks on the western side of the Ailao Shan fault. Fine sericite grains are strongly oriented along major foliations. Fold structures were locally formed by flexural slip of foliations (Figure 6g). Granitic rocks emplaced in the Triassic strata experienced low-temperature deformation. Quartz grains were stretched into ribbon structures (Figure 6h). Different from those in granitic mylonites in the high-grade metamorphic belt, quartz ribbons do not show evidence of dynamic recrystallization, indicating low temperature deformation.

Combining the structural characteristics of the two sections and those from the other parts of the Ailao Shan complex, we could reconstruct the general Cenozoic structural configuration of the Ailao Shan belt as an NW-SE elongated antiformal structure, the Ailao Shan antiform. The high- and low-grade metamorphic belts constitute an antiformal structure that has a hinge line trending NW-SE. The fold structure is well-preserved at the northern end of the Ailao Shan belt, where rocks from the core and the mantles dip oppositely. At the middle and southern part of the complex, e.g., along the Yuanjiang-Mojiang section and other sections further south, the SW limb of the fold is overturned, while the NE limb is lost due to large scale normal faulting along the Red River fault since ca. 5 Ma. The regular changes in decreasing metamorphism and deformation temperatures from the high-grade core to the low-grade limbs with younging stratigraphic horizons along the sections suggest that the crustal section is folded by the Ailao Shan antiform. In addition, the parallelism of the hinge line of the Ailao Shan antiform with stretching lineations of the folded rocks and outcrop scale fold hinges implies that they were formed contemporaneously. Therefore, the Ailao Shan complex exhibits an A-type overturned antiformal structure that was mostly destructed. The SW limb of the fold is well preserved, whereas the NE limb was truncated by the Pliocene Red River fault.

384 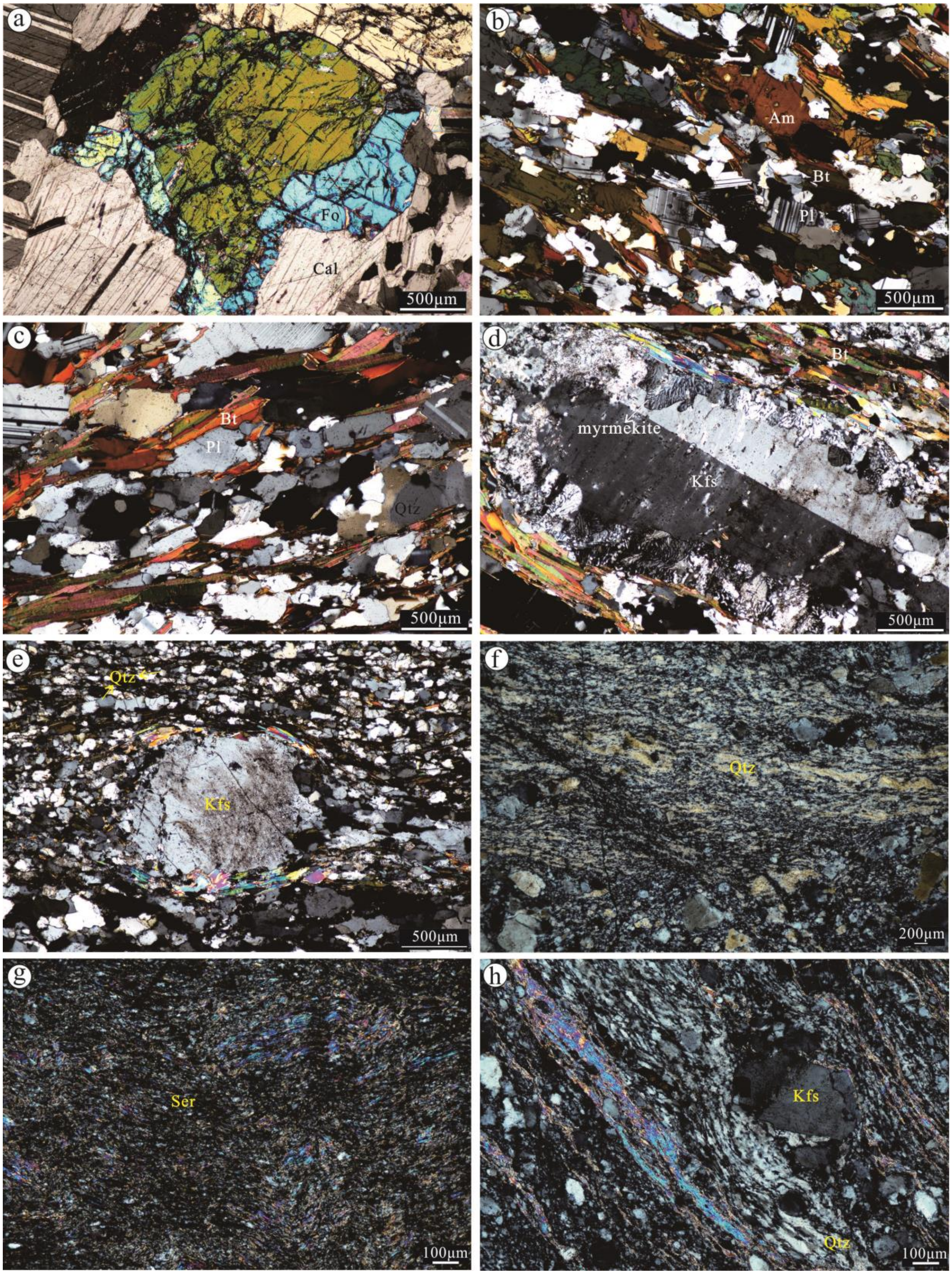

385 **Figure 6.** Microstructures of the Yuanjiang-Mojiang section. a: Forsterite marble. b: In the hornblende biotite
386 plagioclase gneisses, the amphibole and biotite grains are strongly oriented. c: Granitic rocks mostly possess

gneissic structures. d: Myrmekites obviously developed along the rims of K-feldspar grains in high-temperature granitic mylonite. e: Rectangular polycrystalline bands of quartz grains and K-feldspar porphyroclasts. f: Quartz grains were deformed by early stretching into quartz ribbons, and by subsequent subgrain rotation recrystallization during progressive shearing. g: Fine sericite grains are strongly oriented along major foliations, and fold structures were locally formed. h: Quartz grains were stretched into ribbon structures.

3.3 The Yao Shan complex

The Yao Shan- Day Nui Con Voi (YS-DNCV) is the southernmost complex along the ASRR belt (Figure 1). The YS-DNCV complex has an overall elongated configuration with an average width of ca. 20 km and a total length of ca. 350 km, which has two segments, i.e., Yao Shan complex in China (ca. 80 km) and DNCV complex in Vietnam (ca. 270 km) (Figure 7, Anczkiewicz et al., 2007; Chen et al., 2016). The YS-DNCV complex is cut by the Song Chay fault in the east and the Red River fault in the west (Figure 7).

The Yao Shan complex is constituted by three units (Figure 7a), the high-grade core of Paleoproterozoic protoliths (Unit I), the low-grade limbs of Permo-Triassic (Unit II) and a group of low-grade Neoproterozoic-Cambrian rocks (Unit III). The Unit I, forming the core of the complex, is mainly a sequence of metamorphic rocks up to granulite facies (BGMRYP, 1990), including migmatites, sillimanite-garnet gneisses, garnet-biotite gneisses, garnet-biotite schists, and kyanite schists etc., and granitic intrusions of various ages. The rocks were highly sheared (Figures 8a-8d) forming ubiquitous mylonitic fabrics, that the rocks have foliations generally dipping NE, and subhorizontal stretching lineations. Felsic layers in migmatites were sheared into σ porphyrpclasts, indicating top-to-the SE shearing (Figure 8a). Strain localization band locally developed in the granitic mylonite (Figure 8b). Mica fishes in some granitic mylonites forming the S foliation also possess shear senses of top-to-the SE (Figure 8c), and the fine-grained mica and quartz grains oriented along the C foliation (Figure 8c). Myrmekite fabrics locally developed in the rims of K-feldspar porphyroclasts, indicating high-temperature deformation (Figure 8d). Amphibolites and coarse-grained marbles occur locally as interlayers or lenses. The core part was mantled by the Permo-Triassic rocks (Unit II) in the northern part and the Neoproterozoic-Cambrian rocks (Unit III) in the southeast part. The two units belong to the cover succession of the South China block. The Unit II is composed of low-grade metasedimentary and metavolcanics rocks (Figures 8e and 8f, BGMRYP, 1990), including limestones, metabasalts, metasandstones/siltstones, schists, etc. The Unit III is a group of

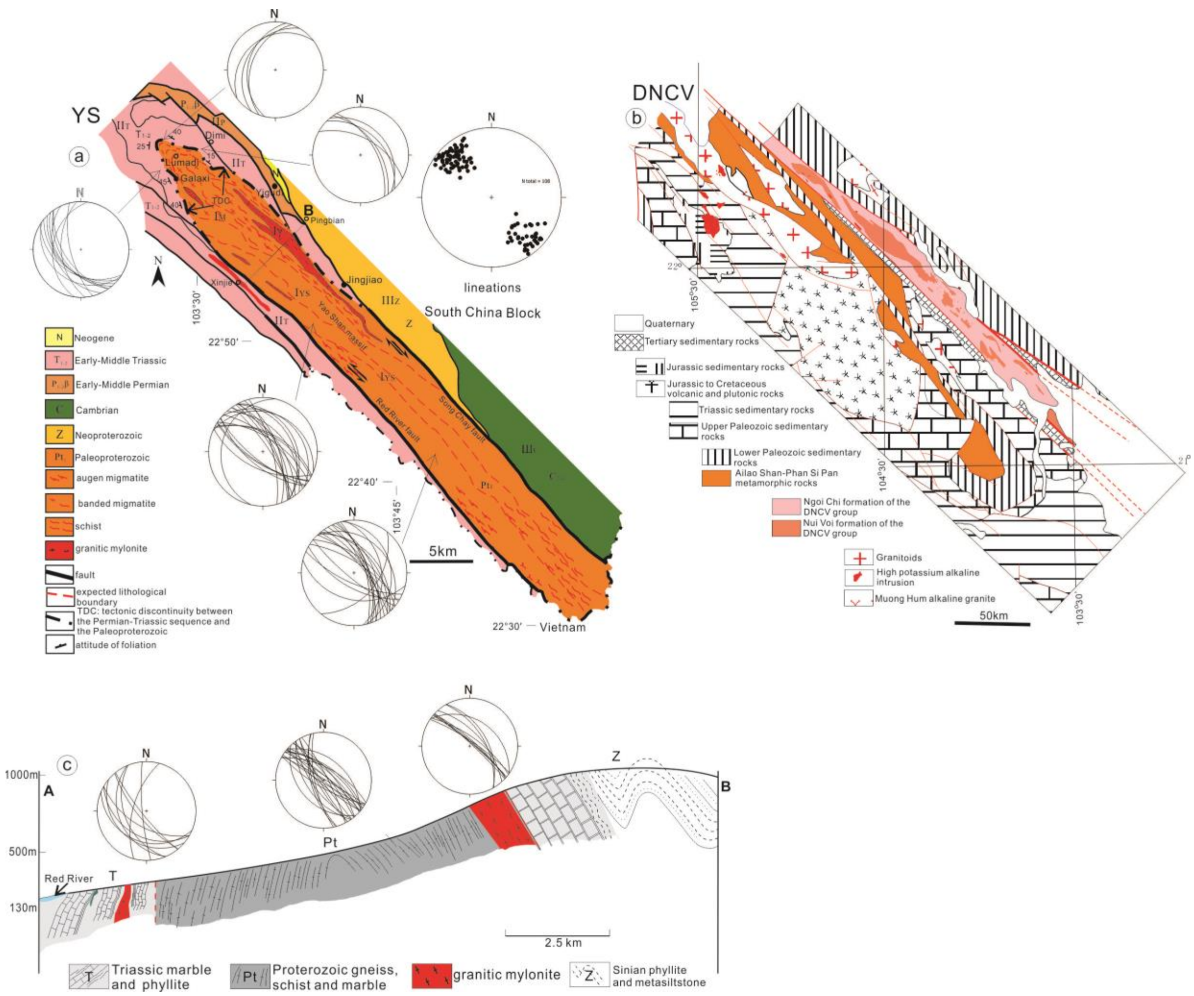

Figure 7. Geological maps of the Yao Shan (a) and Day Nui Con Voi complexes (b). c: Geological section across the Yao Shan complex. Stereonet plots (lower hemisphere, equal-area projections) show the orientations of mylonitic foliations and lineations of the Yao Shan complex.

shallow marine sedimentary rocks (BGMRYP, 1990), including phyllites, siltstones, limestones, etc. The Units II and III are weakly metamorphosed at upper greenschist or lower temperature conditions. The rocks in the two units also experienced ductile deformation, e.g., the composition layers were sheared into asymmetrical lens in marbles (Figure 8e), the oriented and fine-grained sericite grains along the foliations in phyllonites (Figure 8f). Connected with the Yao Shan dome, the core part of DNCV complex is also composed of highly sheared high-grade metamorphic rocks, up to high amphibolite facies, e.g., sillimanite garnet biotite gneisses, diopside graphite gneisses, garner biotite schists, marbles, etc. Locally, high-pressure granulites were exposed as enclaves. The DNCV complex is bounded by the Song Chay fault to the east which is in contact with weakly deformed and low-grade metamorphic or non-metamorphic Lower Paleozoic strata, and by the Red River fault to the west which is in contact with Paleozoic strata and Neogene-Quaternary sediments.

The structural geology of the Yao Shan complex is characterized by a first-order linear NW-plunging antiformal structure, plunging at the northwest of Galaxi village. The structure extends southwards to DNCV in NW–SE direction. The distribution of Unit I and Triassic rocks of Unit II outlines the antiformal structure (Figure 7a). Field observations suggest that the contact between Unit I and Units II-III is a shear discontinuity (TDC, Chen et al., 2016). Along and on both sides of the contact, the rocks from Units I and II were intensively sheared into mylonites. The foliations and lineations in the rocks of the two units exhibit parallel relationships and identical kinematics. At localities where the contact is exposed, neither brittle faults nor evidences of unconformity are observed (Chen et al., 2016). The foliations mainly strike NW-SE, paralleling with the striking of the Yao Shan complex. The two limbs dip oppositely in the northern segment. However, the foliations mainly dip to NE in the southern segment, revealing a locally overturned monoclinal structure. The stretching lineations in the sheared rocks from different units mainly plunges to NW or SE, implying that the three units constitute a regional A-type antiformal structure plunging NW. The antiformal structure is bounded and destructed by the steeply dipping Song Chay and Red River faults (Anczkiewicz et al., 2007). The mylonitic foliations run almost parallel to the striking of the DNCV fold hinge in NW-SE direction.

Granitic intrusions in the YS-DNCV complexes are not as common as in the Ailao Shan complex. There are two Cretaceous large plutons with surface outcrop patterns striking along the Yao Shan complex, and several small intrusions of various ages at the map and outcrop scales (Figure 7a). Zircon U-Pb and εHf(t) ages of the granitic intrusions in the Yao Shan complex show that Yao Shan complex records evidences of extensive partial melting of the Precambrian crystalline basement rocks (Chen et al., 2017b, 2019). A group of syn-shearing granitic dykes at Oligocene magmatic ages have been acquired, i.e., a sheared granitic dyke with age of 29.42±0.54 Ma intruding the mylonitic paragneiss (Chen et al., 2016), a two-mica granitic dyke with age of 30.65±0.41 Ma intruding the Triassic marble (Chen et al., 2016), a granitic dyke with age of 31.44±0.53 Ma intruding the Proterozoic paragneiss (Chen et al., 2016). Previous studies revealed that the formation of the ~30 to ~20 Ma granites is associated with ductile shearing along the ASRR tectonic belt (Cao et al., 2011a; Tang et al., 2013). $^{40}Ar/^{39}Ar$ dating of hornblende, mica, and K-feldspar from the leucogranite, pegmatite, gneiss, and amphibolite in the core part of DNCV complex yielded ages of 23.7–33.8 Ma, 21.2–24.8 Ma, and 18.4–24.3 Ma, respectively (Wang et al., 1998). They yield a very slow cooling ca. 34–25 Ma in the late Paleogene and a rapid cooling in the early Miocene (25–21 Ma).

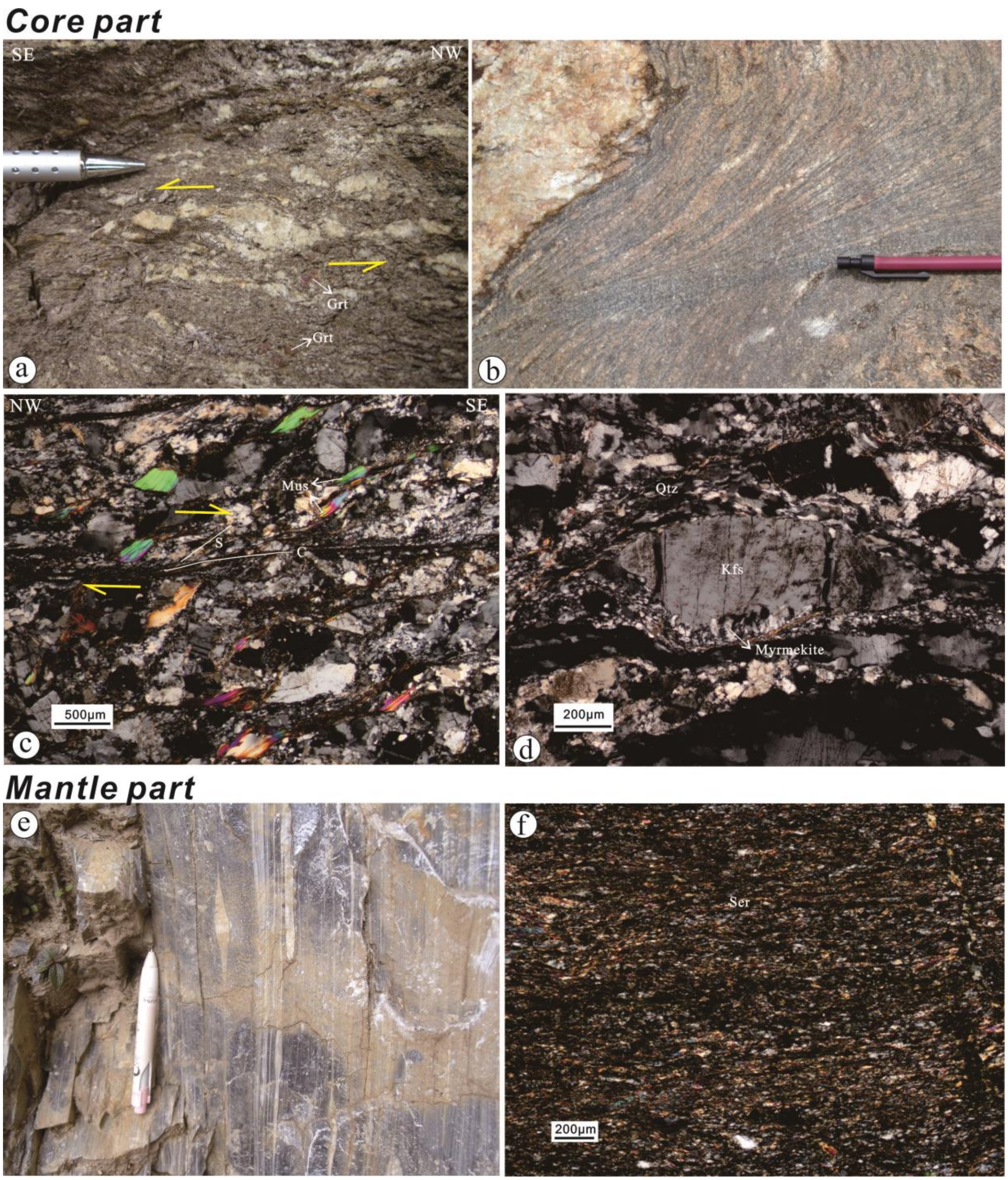

Figure 8. Macro- and micro- structures of the rocks from the core and mantle parts of the Yao Shan complex. a: Felsic layers in migmatites from the northern part of the complex were sheared into σ porphyrpclasts, indicating top-to-the SE shearing. b: Stain localization band in the migmatic granite. c: Mica fishes in some granitic mylonites from the northern part of the complex indicate shear senses of top-to-the SE, fine-grained quartz and mica grains oriented along the foliation. d: Myrmekite developed along the margins of K-feldspar

grains. e: The composition layers were sheared into asymmetrical lens. f: Oriented and fine-grained sericite grains along the foliation in phyllonite.

3.4 The Xuelong Shan complex

The Xuelong Shan complex is the northernmost complex along the ASRR belt (Figure 1), extending NW-SE with elliptical surface exposure of about 50 km long and 2 ~ 8 km wide. The complex exhibits a dome shaped structure that is cored by Paleo-Proterozoic high-grade metamorphic gneisses and granitic intrusions of various ages, and mantled by Triassic-Cretaceous low-grade metamorphic rocks (Figure 9, Zhang et al., 2014). The gneissic core is composed of orthogneisses and paragneisses, which locally experienced migmatization. The low-grade metamorphic rocks, including mica schists, mica quartz schists, plagioclase amphibole schists, marbles, quartzites, etc., are distributed around the core. Rocks from both the core and mantle parts were highly sheared and transformed into mylonitic rocks. Mylonitic foliations strike NW-SE, and constantly dip to NE along the NE flank and to the SW along the SW flank, which supports the conclusion of existence of a dome structure. Stretching lineations in the sheared rocks are generally sub-horizontal, plunging to N or S (Figure 9, Zhang et al., 2014).

Zhang & Schärer (1999) suggested that the Xuelong Shan complex suffered at least two periods of granite emplacement: a first stage of Early Cenozoic (70-50 Ma) and a second stage of about 33 Ma. Leucocratic layers emplaced during shearing at 33 Ma subsequently suffered ductile deformation. The biotite $^{40}Ar/^{39}Ar$ dating of mica schist from the core part yields plateau age of 28.2 ± 0.6 Ma (Leloup et al., 2001). The muscovite $^{40}Ar/^{39}Ar$ dating from orthogneiss boulder yields plateau age of 30.0 ± 0.6 Ma (Leloup et al., 2001). Apatite fission track dating from a gneiss boulder yields an age of 2.7 ± 0.6 Ma (Bergman et al., 1997). Leloup et al. (2001) obtained cooling path of the Xuelong Shan complex based on the thermal chronology data, showing that the complex experienced a relatively rapid cooling and exhumation between 33 to 26Ma, that was followed by a relatively slow cooling (Zhang & Schärer, 1999).

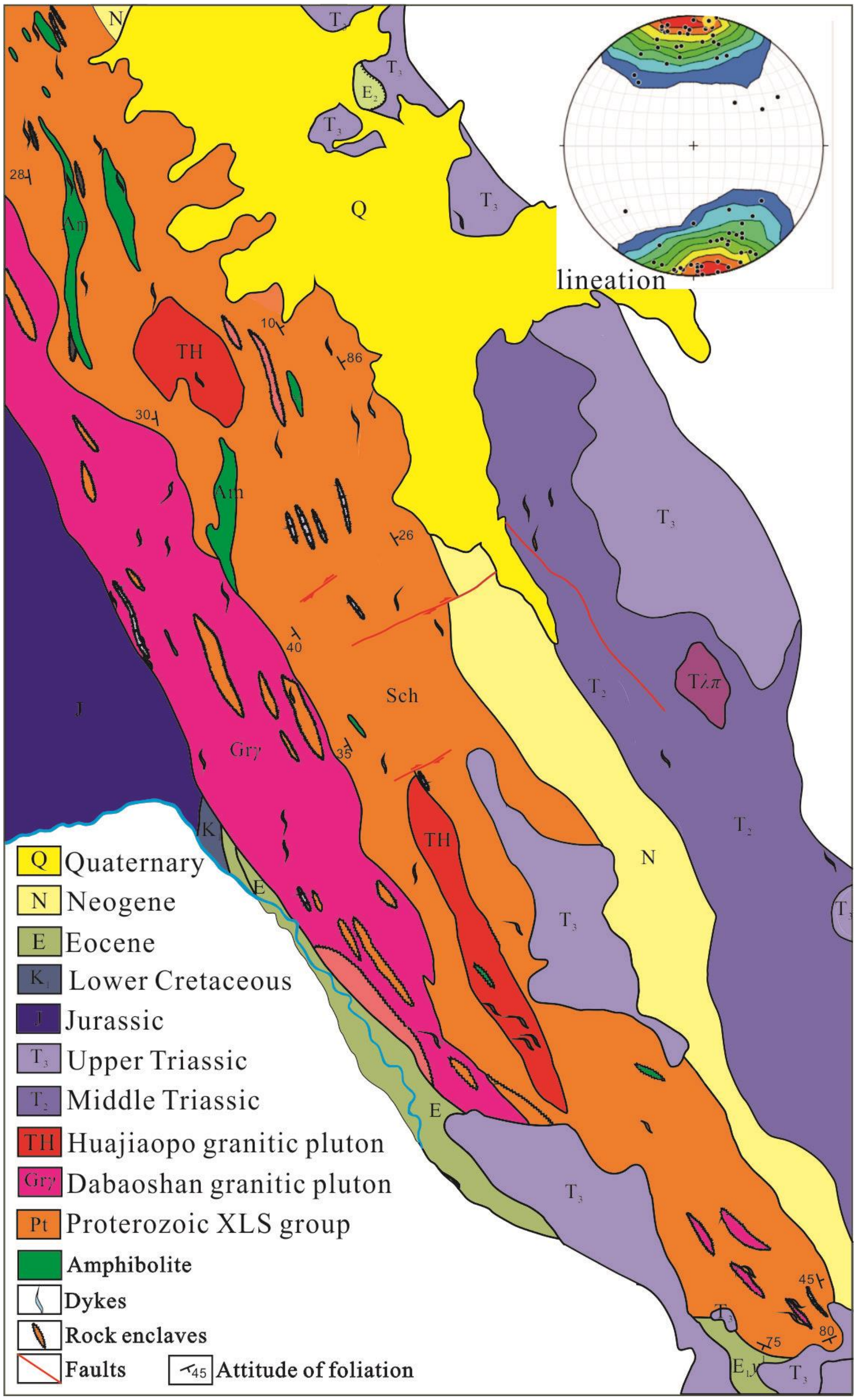

Figure 9. Geological map of the Xuelong Shan complex.

3.5 The Ximeng complex

The Ximeng complex is located in the eastern part of the Sibumasu block, and to the west of the Changning-Menglian suture zone (Figure 1). The complex strikes NNW-SSE with an elliptical surface shape and extends northward into Burma (Figure 10). The macroscopic structural configuration of the Ximeng complex is a dome structure. The core part is composed of highly sheared Neoproterozoic metamorphic rocks, and Early Paleozoic granitic intrusions. The Neoproterozoic metamorphic rocks were metamorphosed up to the garnet grade of the Barrovian metamorphic belt. Two mica quartz schists, garnet bearing schists, marbles, are exposed in the eastern and southern part of the complex. The large-scale Laojiezi granitic pluton (430-465 Ma, Chen et al., 2017a) was exposed in the northern and central part of the core. The main rock type is fine- to medium- grained porphyritic tourmaline-bearing mica granite with mineral compositions of quartz + K-feldspar + plagioclase + muscovite/bitote + tourmaline (Figures 11a-11c, Chen et al., 2017a). Mylonitic foliations, stretching lineations and porphyroclastic fabrics were well developed in the sheared granitic rocks (Figures 11a-11c). Most of the K-feldspar porphyroclasts show shear senses of top-to-the SE shearing (Figures 11b). In the granitic mylonites, quartz grains are in the form of rectangular quartz bands, and fine-grained K-feldspar grains are intervening with the quartz bands, possibly related to high-temperature deformation (Figure 11c). The quartz grains in muscovite quartz schists exhibit rectangular quartz bands. Locally, grain boundary migration are observed. The oriented muscovite grains define the mylonitic foliations (Figure 11d). Mica fishes in the rocks show shear senses of top-to-the S shearing (Figure 11e). In the sheared marble, strain localization band developed locally with obvious grain size reduction of calcite grains (Figure 11f). The core part is mantled by highly sheared Cambrian sedimentary sequences, including phyllites, metasiltstones and crystalline limestones. Shearing occurred at low-grade metamorphic conditions up to greenschist facies (Figures 11g and 11h, Chen et al., 2017a). It is shown that the sheared metasedimentary rocks in the core and mantle have mineral assemblages for distinctive metamorphic grades. However, mylonitic foliations and lineations in the two units show parallel relationships and identical kinematics (Chen et al., 2017a), suggesting that a shear discontinuity exists between the two units (Chen et al., 2017a).

Foliations at different parts of the dome dip away from the core in various directions with small dip angles. However, the plunging of the stretching lineation is quite stable and keep consistent at different parts of the Ximeng dome, in either NWN or SES orientations (Figure 10). The development of the varying attitudes of mylonitic foliations and consistent stretching lineations suggests that the dome was formed coevally with the mylonitic fabrics, which are attributed to regional A-type folding or doming (Chen et al., 2017a).

$^{40}Ar/^{39}Ar$ dating was performed on muscovite, biotite, K-feldspar minerals from the Laojiezi granitic mylonites in the core part and yielded ages of 21-23 Ma, 22 Ma, and 15-20 Ma, respectively (Chen et al., 2017a). Three apatite from the same samples yielded fission track ages of 9-12 Ma. Two stages cooling history for the Ximeng complex was constructed which consists of an early rapid cooling (~112.6℃/Ma) from 20-23 Ma then followed by a late slow cooling (7.5–16.9 ℃/Ma).

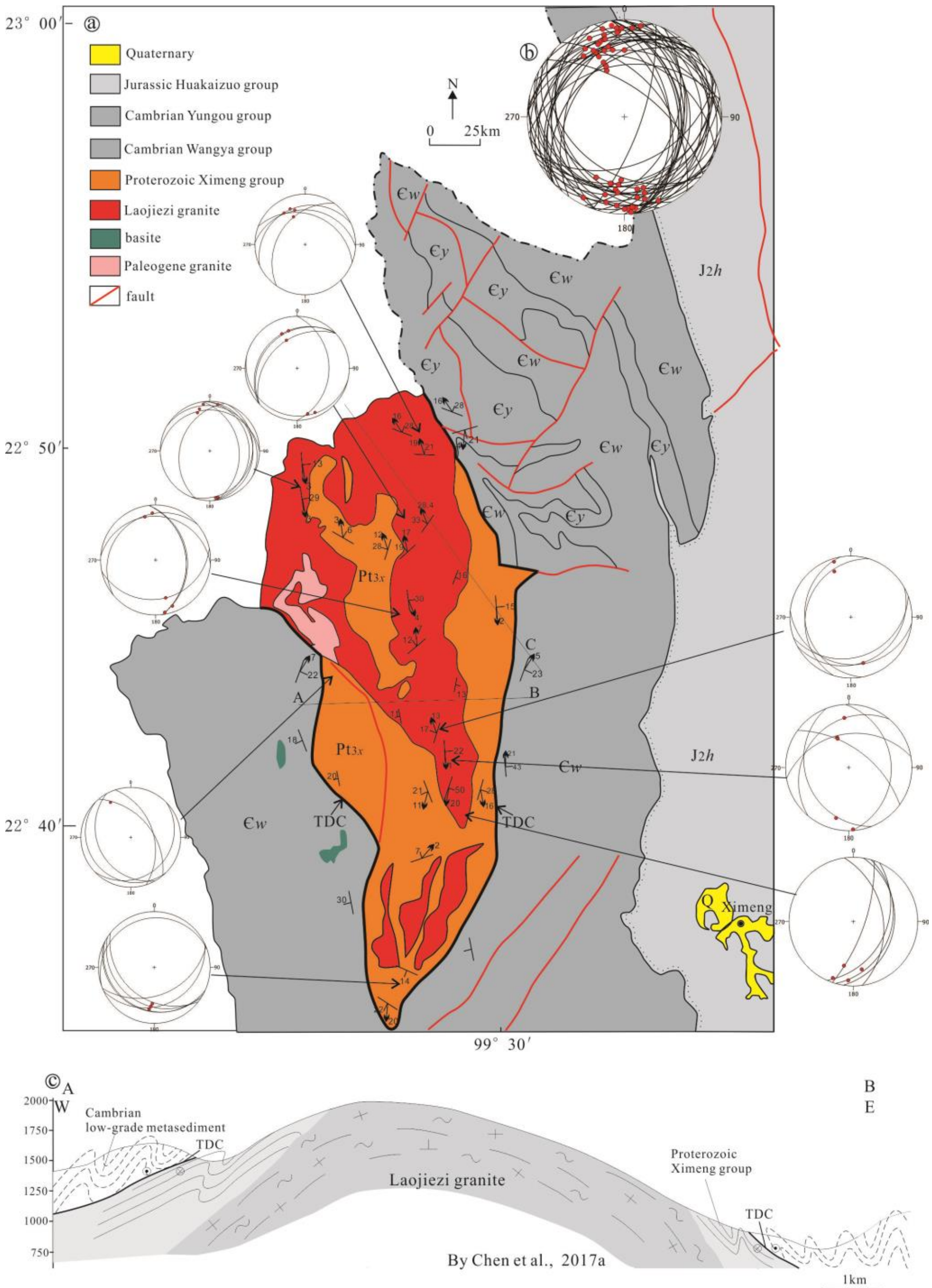

Figure 10. Geological map of the Ximeng complex, showing stereographic projections (lower hemisphere, equal area) of foliations and stretching lineations for specific localities (a) and for the entire complex (b). (c) Geological section along the AB profile (Modified after Chen et al., 2017a).

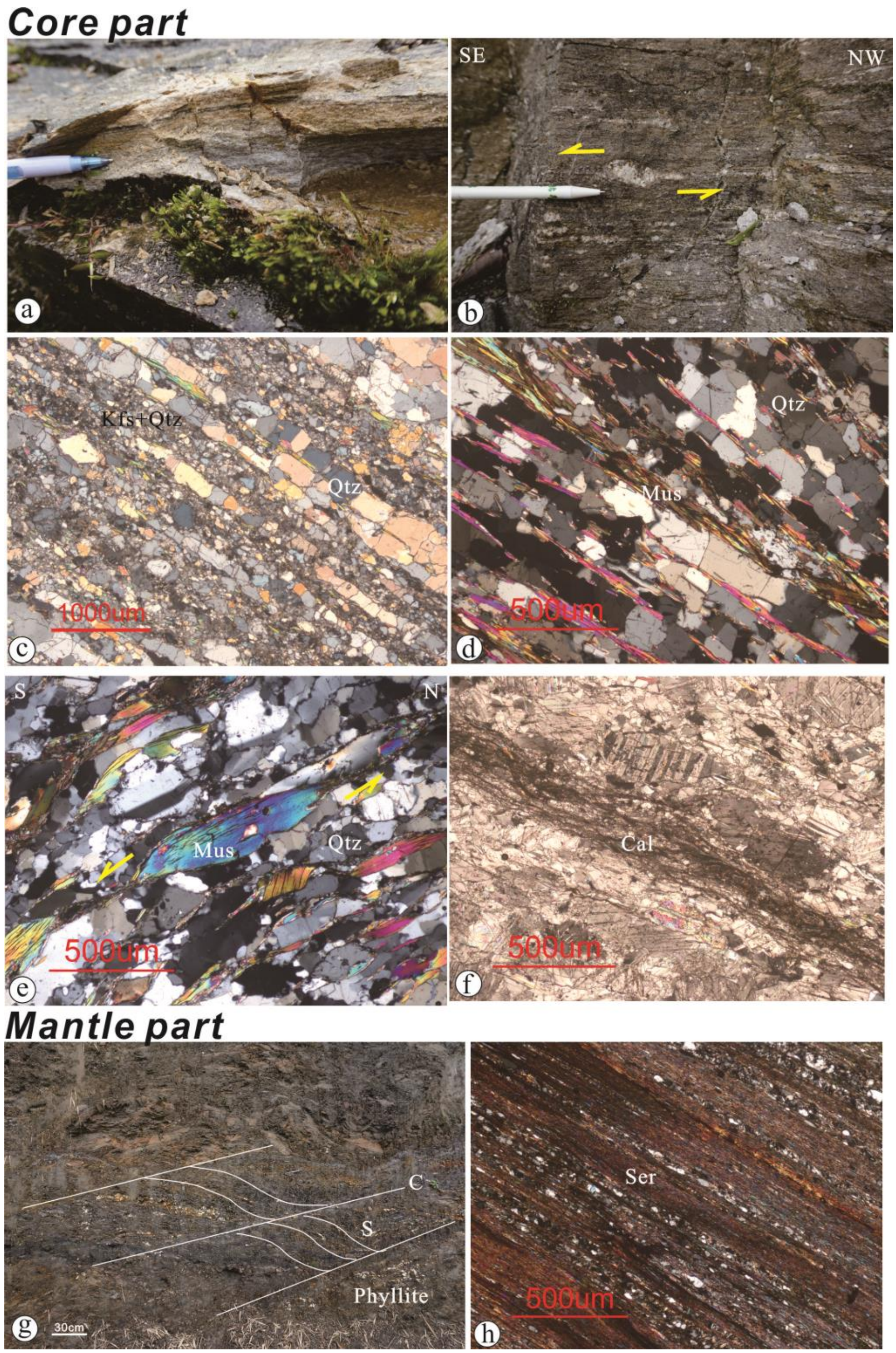

545

Figure 11. Macro- and micro- structures of the rocks from the core and mantle parts of the Ximeng complex. a: Mylonitic foliations in the Laojiezi granite pluton. b: K-feldspar porphyroclasts indicate top-to-the SE shearing. c: Rectangular quartz bands caused by static

recovery, and fine-grained feldspar and quartz grains attributed to bulging recrystallization. d: Mica fishes in the rocks show shear senses of top-to-the S shearing. e: Static recovery of quartz grains in the biotite schist. f: Calcite grains experienced recrystallization and elongation. g: Sheared phyllite forming the SC fabric. h: Cambrian phyllite experienced ductile shearing forming cleavage domains and microlithons.

3.6 The Gaoligong complex and Tengchong gneiss domes

The Gaoligong complex is a N-S trending belt in the northern segment and changes to NE-SW trending in the south segment (Figs. 1 and 12), with ~10 km in width and 600 km in total length. The complex is located on the west side of Nujiang fault, and extends from the SE side of the east Himalayan Syntaxis into the Burma Mogok massif southward. The Gaoligong complex is mainly composed of strongly deformed metamorphic rocks, including sillimanite garnet biotite gneisses, biotite amphibolite plagioclase gneisses, amphibolites, granulites, migmatites, and granites, etc. Pervasive mylonitic foliations are widely developed, striking NWN-SES in the north segment and NE-SW in the south segment, both with steep dip angles (Zhang et al., 2017). The stretching lineations are quite stable plunging to NWN or SES in the north segment, and NE-SW in the south segment, both with small plunge angles (Zhang et al., 2017). The zone is characterized by a large-scale first-order antiform (Zhang et al., 2012). According to the stereogram plot of the mylonitic foliations and stretching lineations published in Zhang et al. (2012), the fold axes, namely the intersection of the mylonitic foliations, are consistent with the stretching lineations, suggesting that the complex is a large-scale A-type antiform. In the Tengchong terrane, four elongated domes are well exposed, i.e., the Sudian, Yinjiang, Guyong, and Lianghe domes, oriented in N-S to NE-SW direction (Figure 12, Zhang et al., 2017). These domes are cored by high-grade metamorphic rocks and granite plutons, mantled by 4-10 km thick gneiss sheets (Zhang et al., 2017), and bounded by NE-trending strike-slip shear zones (Xu et al., 2015).

$^{40}Ar/^{39}Ar$ dating of hornblende, biotite and muscovite grains from the granitic mylonite, amphibolite, and mica schist yields ages of 23-33.7 Ma, 10-28.4 Ma and 16.2-32.7 Ma, respectively (Table S1). Biotite $^{40}Ar/^{39}Ar$ ages of syn-shearing granitic mylonites are 15-16 Ma. Weakly deformed leucogranite and protomylonite yield $^{40}Ar/^{39}Ar$ ages of 10-11 Ma, indicating that ductile shearing related to the escape of the Sundaland block continued to the Late Miocene (Zhang et al., 2012).

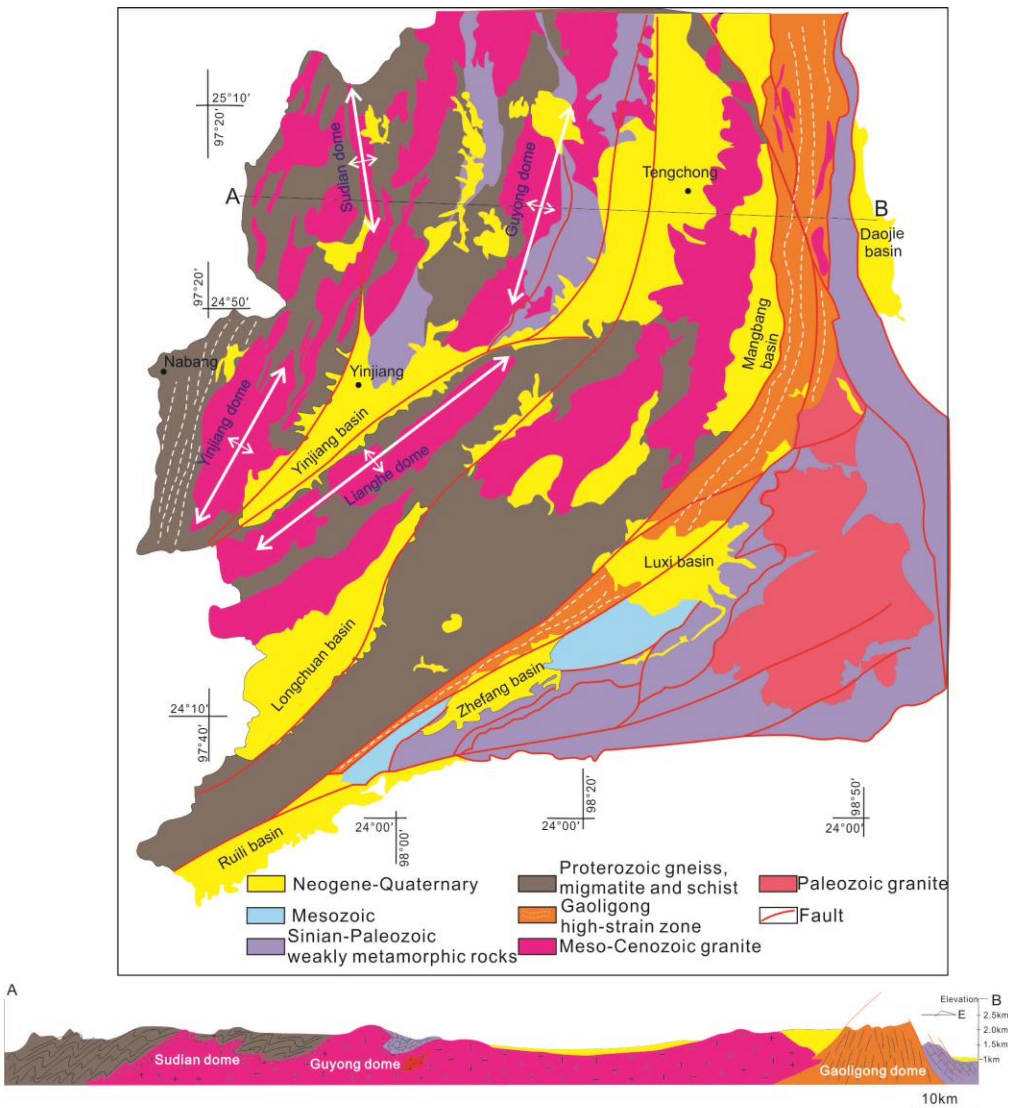

Figure 12. Geological map of the southern Gaoligong belt and the adjacent gneiss domes and the profile (Modified after Zhang et al., 2017).

4 Zircon U-Pb dating of the syn-kinematic dykes and timing of deformation

Oligocene–Miocene leucocratic intrusions are common in the high-grade unit, but are rare in the low-grade unit (Searle et al., 2010). Based on structural, microstructural, and fabric analyses, they were grouped into pre-, syn-, and post- kinematic intrusions in relation to the ductile shearing (Liu et al., 2020; Searle et al., 2010). One example of the syn-kinematic dykes in the southern Diancang Shan complex (Figure 13a), the leucocratic dykes are obviously mylonitized, and the occurrence of the foliation is consistent with that of the surrounding rocks. The dikes underwent two stages of folding, forming rootless, intrafolia folds. The early folding (F_1^1) is characterized by the development of axial foliation (S_1^1) paralleling with the surrounding rocks, while the late folding (F_1^2) is characterized by the flexural folding of foliations in both the surrounding rocks and dykes (Figure 13a). The leucocratic dykes experienced the early and late stages of shear deformation. In another example of syn-shearing dykes, the dyke truncated the foliations of the surrounding rocks, but experienced mylonitization and formed foliations that are consistent with those in the surrounding rocks (Figure 13b). Eight granitic mylonites from the Diancang Shan complex were sampled according to the above criteria for syn-shearing dykes, and dated with laser ablation-inductively coupled plasma–mass spectrometry (LA-ICP-MS) techniques in this study. For analytical techniques applied in the present study, refer to the supplementary material Appendix. The dating results are shown in Table 1.

601 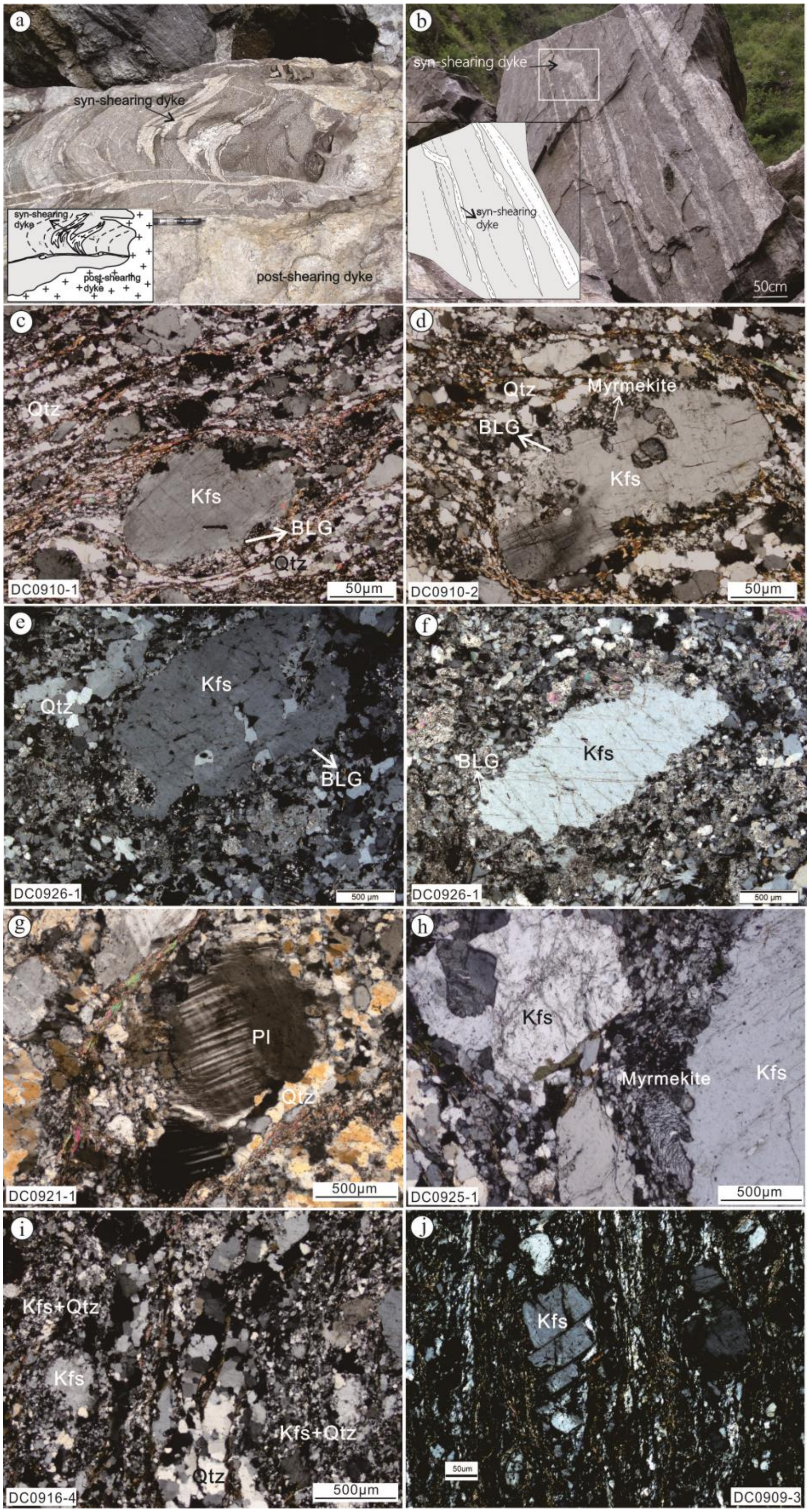
a
syn-shearing dyke
syn-shearing dyke
post-shearing dyke
post-shearing dyke
b
syn-shearing dyke
syn-shearing dyke
50cm
c
Qtz
Kfs
BLG
Qtz
DC0910-1
50μm
d
Qtz
Myrmekite
BLG
Kfs
DC0910-2
50μm
e
Kfs
Qtz
BLG
DC0926-1
f
Kfs
BLG
DC0926-1
g
Pl
Qtz
DC0921-1
500μm
h
Kfs
Myrmekite
Kfs
DC0925-1
500μm
i
Kfs+Qtz
Kfs
Kfs+Qtz
Qtz
DC0916-4
500μm
j
Kfs
DC0909-3

Figure 13. Macro- and micro- structures of the granitic dykes from the Diancang Shan complex. a: Syn-shearing dykes suffered from progressive shearing. b: Syn-shearing dyke: truncate the foliation of the surrounding rocks and were also transformed forming mylonitic foliation that parallel with the surrounding rocks. c-f: K-feldspar porphyroclasts that experienced bulging recrystallization, quartz grains are in the form of polycrystalline bands. g: Plagioclase porphyroclast with quartz aggregates around it. h: K-feldspar porphyroclast with myrmekite structure around it. i: Polycrystalline quartz bands, the K-feldspar porphyroclasts experienced obvious bulging recrystallization with fine grained K-feldspar grains along the foliation. j: Domino structure of the K-feldspar porphyroclast and quartz ribbons along the mylonitic foliation. BLG: Bulging recrystallization.

Samples DC0910-1 and DC0910-2 are biotite granitic mylonites which are characterized by round-shaped K-feldspar porphyroclasts and quartz polycrystalline bands (Figures 13c and 13d). The K-feldspar porphyroclasts experienced obvious bulging recrystallization around their margins. Fine-grained feldspar and quartz grains are distributed around the feldspar porphyrpclasts. Biotite grains were sheared into fine grains along the mylonitic foliations (Figures 13c and 13d). DC0926-1 is a two-mica granitic mylonite, K-feldspar grains are in the form of porphyroclasts with bulging recrystallization grains around the margins. However, some of the K-feldspar porphyroclasts still retain the platy crystal shape, showing the characteristics of magmatic crystallization and plastic deformation during shearing (Figures 13e and 13f). Quartz grains are in the form of polycrystalline quartz bands (Figure 13f). DC0921-1 is a biotite granitic mylonite, K-feldspar and plagioclase grains are in the form of porphyroclasts. Quartz grains exhibit triple junction (Figure 13g). DC0925-1 is a biotite granitic mylonite, K-feldspar grains were sheared into porphyroclasts with myrmekite and bulging recrystallization developed around the margins. Quartz grains are in the form of polycrystalline aggregation. Oriented biotite grains define the mylonitic foliation (Figure 13h). DC0916-4 is a biotite granitic mylonite, the K-feldspar porphyroclasts experienced obviously bulging recrystallization, only relics of K-feldspar porphyroclasts could be observed. The recrystallized feldspar grains distributed along the mylonitic foliations. Quartz grains are in the form of polycrystalline quartz bands. Biotite grains were oriented between these bands (Figure 13i). DC0909-3 is a biotite granitic mylonite, the K-feldspar porphyroclasts show domino structures, whereas the quartz grains were stretched forming quartz ribbons that define the mylonitic foliations (Figure 13j). These deformation microstructures suggest that most of the samples underwent medium-high temperature deformation (550-600℃). Only sample DC0909-3 records the late-stage superposition of low-temperature deformation.

The zircon grains acquired from the sample DC0910-1 show euhedral to subhedral shapes (Figure 14h), with aspect ratios between 1:1 and 3:1 and lengths up to 150 μm. The CL images exhibit characteristics of hydrothermal alteration in the cores and latest magmatic growth rims (Figure 14h). Eight laser spots were analyzed on the growth rims for this sample. The analyzed zircons have Th contents of 257–1380 ppm, U contents of 7860–15007 ppm. The analyses yield a weighted mean $^{206}Pb/^{238}U$ age of 23.22 ± 0.22 Ma (MSWD=2.2) (Figure 14a), which is interpreted to be the igneous age. Zircon grains from the sample DC0910-2 are euhedral shapes, with oscillatory zonings throughout the whole grains (Figure 14i). The grains have aspect ratios between 1:1 and 4:1. Most of the rims are darker than the cores, indicative of high U content in the rims. 14 laser spots were analyzed on the rims. The analyzed zircons have Th contents of 177–5233 ppm, U contents of 451–13753 ppm. The analyses yield a weighted mean $^{206}Pb/^{238}U$ age of 27.40 ± 0.19 Ma (MSWD=2.0) (Figure 14b), interpreted to be the crystallization age for the rock. Zircon grains from the sample DC0926-1 are euhedral shapes (Figure 14j). Most of the zircons have oscillatory zonings throughout the whole grains. Only few zircons have inherited cores. The grains have aspect ratios between 1:1 and 5:1. 16 laser spots were analyzed on the rims of oscillatory zonings. These data have Th contents of 798–3597 ppm,

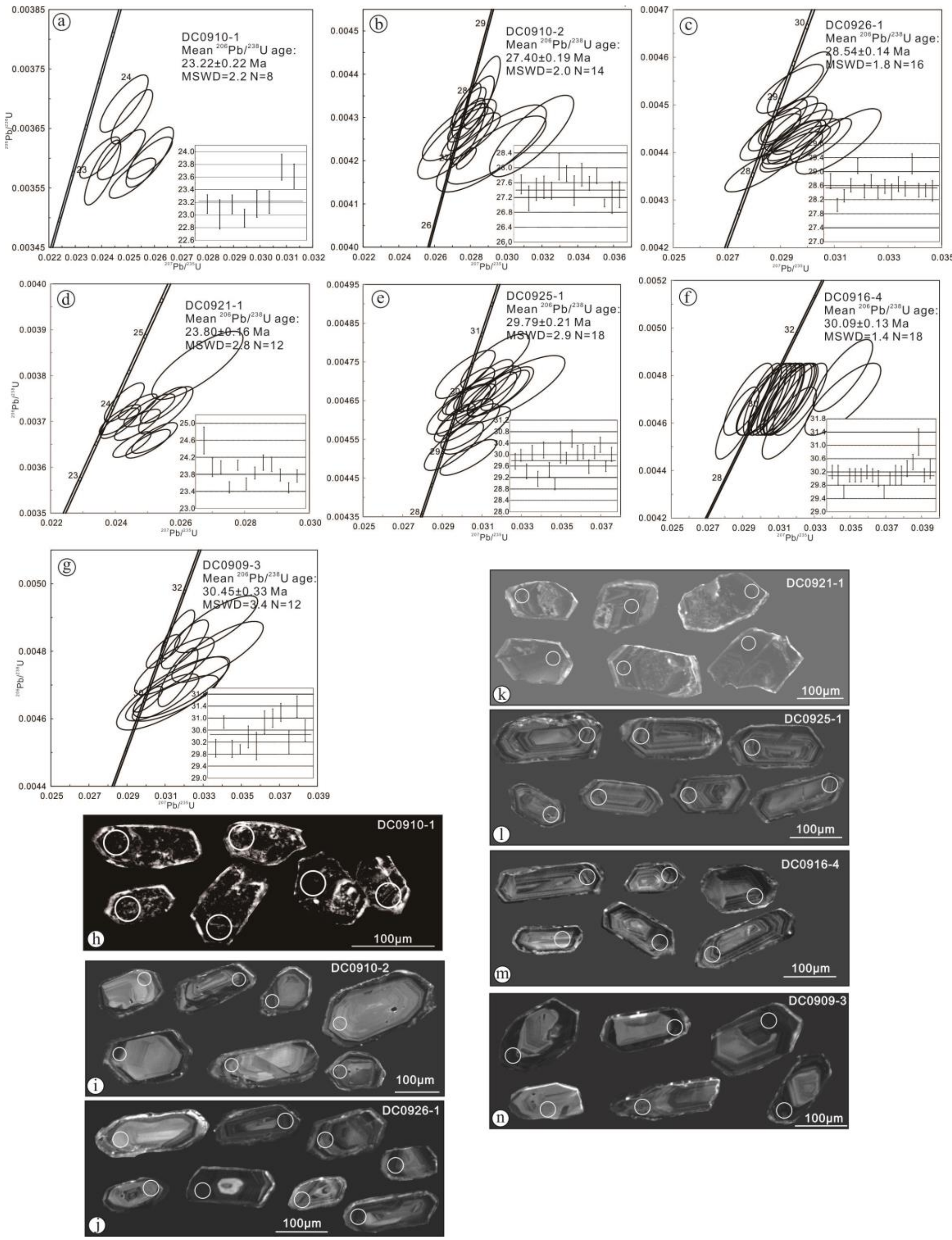

Figure 14. LA-ICP-MS U-Pb concordia diagrams (a–g) and cathodoluminescence (CL) images of representative zircons (h–n) from the dated granitic samples from the Diancang Shan complex. Circles indicate spots of the LA-ICP-MS dating.

U contents of 1904–7495 ppm. The weighted mean $^{206}Pb/^{238}U$ age of 28.54 ± 0.14 Ma (MSWD=1.8) should represent the age of crystallization (Figure 14c). Most of the zircon grains from the sample DC0921-1 are euhedral to subhedral shapes (Figure 14k). They have aspect ratios between 1:1 and 2:1, and lengths of ~200 μm. The core parts experienced obvious hydrothermal alteration with magmatic growth rims in the CL images (Figure 14k). 12 laser spots were analyzed on the rims of oscillatory zonings. Analyses of zircon grains have Th contents of 360–1644 ppm, U contents of 11648–33939 ppm. Most of the analytical population is concordant, producing a weighted mean $^{206}Pb/^{238}U$ age of 23.80 ± 0.16 Ma (MSWD = 2.8) (Figure 14d), interpreted to be the crystallization age for the rock. Zircon grains from the sample DC0925-1 are euhedral shapes, with oscillatory zonings throughout the whole grains (Figure 14l). The grains have aspect ratios between 1:1 and 5:1, and lengths of ~300 μm. 18 laser spots were analyzed on the rims of oscillatory zonings. These data have Th contents of 223–2132 ppm,

Table 1 Zircon U-Pb LA-ICP-MS data of the granitic rocks from the Diancang Shan complex.

spot number	Content		Th/U	Isotopic ration						Age (Ma)			
	Th	U		$^{207}Pb/^{206}Pb$	1σ	$^{207}Pb/^{235}U$	1σ	$^{206}Pb/^{238}U$	1σ	$^{207}Pb/^{235}U$	1σ	$^{206}Pb/^{238}U$	1σ
DC0910-1													
DC0910-1-01	580	13423	0.04	0.0480	0.0010	0.0239	0.0005	0.0036	0.0000	24.0	0.5	23.2	0.1
DC0910-1-02	257	9204	0.03	0.0488	0.0010	0.0240	0.0005	0.0036	0.0000	24.1	0.4	23.0	0.2
DC0910-1-06	404	10795	0.04	0.0519	0.0012	0.0258	0.0006	0.0036	0.0000	25.9	0.6	23.2	0.1
DC0910-1-11	1380	15007	0.09	0.0510	0.0012	0.0252	0.0006	0.0036	0.0000	25.2	0.6	23.0	0.1
DC0910-1-12	361	7964	0.05	0.0517	0.0011	0.0258	0.0006	0.0036	0.0000	25.9	0.6	23.2	0.2
DC0910-1-17	287	7860	0.04	0.0497	0.0012	0.0247	0.0006	0.0036	0.0000	24.8	0.6	23.2	0.2
DC0910-1-20	479	9454	0.05	0.0489	0.0012	0.0249	0.0006	0.0037	0.0000	24.9	0.6	23.8	0.2
DC0910-2													
DC0910-2-1	1568	6732	0.23	0.0470	0.0011	0.0278	0.0007	0.0043	0.0000	27.8	0.7	27.6	0.3
DC0910-2-2	253	720	0.35	0.0505	0.0030	0.0294	0.0018	0.0042	0.0001	29.5	1.8	27.2	0.3
DC0910-2-6	774	8387	0.09	0.0473	0.0010	0.0278	0.0006	0.0043	0.0000	27.9	0.6	27.4	0.3
DC0910-2-7	416	917	0.45	0.0465	0.0024	0.0274	0.0014	0.0043	0.0000	27.4	1.3	27.5	0.3
DC0910-2-8	882	1484	0.59	0.0479	0.0019	0.0280	0.0011	0.0043	0.0000	28.1	1.1	27.4	0.2
DC0910-2-9	2162	9029	0.24	0.0474	0.0009	0.0287	0.0007	0.0044	0.0001	28.7	0.7	28.0	0.4
DC0910-2-10	1098	11916	0.09	0.0464	0.0009	0.0278	0.0005	0.0043	0.0000	27.8	0.5	27.8	0.2

DC0910-2-13	259	780	0.33	0.0541	0.0027	0.0314	0.0016	0.0043	0.0001	31.4	1.5	27.4	0.4
DC0910-2-14	1670	5533	0.30	0.0471	0.0012	0.0282	0.0008	0.0043	0.0000	28.2	0.8	27.8	0.3
DC0910-2-15	1321	5043	0.26	0.0471	0.0012	0.0279	0.0007	0.0043	0.0000	27.9	0.7	27.6	0.2
DC0910-2-19	1965	4546	0.43	0.0464	0.0010	0.0279	0.0007	0.0043	0.0000	27.9	0.6	27.8	0.2
DC0910-2-20	5233	13753	0.38	0.0478	0.0006	0.0278	0.0004	0.0042	0.0000	27.8	0.4	27.1	0.1
DC0910-2-22	177	451	0.39	0.0516	0.0037	0.0292	0.0020	0.0042	0.0001	29.2	2.0	27.2	0.4
DC0910-2-23	307	833	0.37	0.0468	0.0025	0.0272	0.0014	0.0042	0.0001	27.2	1.4	27.3	0.4
DC0926-1													
DC0926-1-01	2367	5300	0.45	0.0474	0.0012	0.0293	0.0007	0.0045	0.0000	29.3	0.7	28.7	0.2
DC0926-1-02	2642	5829	0.45	0.0467	0.0013	0.0282	0.0008	0.0044	0.0000	28.2	0.8	28.0	0.2
DC0926-1-03	1373	4828	0.28	0.0484	0.0013	0.0294	0.0008	0.0044	0.0000	29.4	0.8	28.3	0.2
DC0926-1-04	3411	7495	0.46	0.0468	0.0011	0.0288	0.0006	0.0044	0.0000	28.8	0.6	28.6	0.2
DC0926-1-05	1823	4544	0.40	0.0469	0.0014	0.0294	0.0008	0.0045	0.0000	29.4	0.8	29.2	0.2
DC0926-1-08	2328	4844	0.48	0.0481	0.0012	0.0294	0.0007	0.0044	0.0000	29.4	0.7	28.4	0.2
DC0926-1-09	2995	6041	0.50	0.0472	0.0009	0.0291	0.0006	0.0045	0.0000	29.2	0.6	28.7	0.2
DC0926-1-11	1514	4310	0.35	0.0487	0.0013	0.0297	0.0008	0.0044	0.0000	29.7	0.8	28.4	0.2
DC0926-1-12	1559	4127	0.38	0.0486	0.0012	0.0298	0.0008	0.0044	0.0000	29.8	0.7	28.6	0.2
DC0926-1-13	798	2276	0.35	0.0489	0.0016	0.0298	0.0010	0.0044	0.0000	29.8	0.9	28.4	0.2
DC0926-1-14	2127	4689	0.45	0.0481	0.0012	0.0296	0.0008	0.0045	0.0000	29.6	0.7	28.6	0.2
DC0926-1-15	2254	5029	0.45	0.0467	0.0012	0.0286	0.0007	0.0044	0.0000	28.7	0.7	28.5	0.2

DC0926-1-17	1210	4265	0.28	0.0472	0.0012	0.0297	0.0008	0.0045	0.0000	29.7	0.8	29.2	0.3
DC0926-1-18	3597	6627	0.54	0.0498	0.0012	0.0305	0.0007	0.0044	0.0000	30.5	0.7	28.5	0.2
DC0926-1-19	2239	5216	0.43	0.0483	0.0012	0.0296	0.0007	0.0044	0.0000	29.6	0.7	28.5	0.2
DC0926-1-20	1044	1904	0.55	0.0514	0.0018	0.0311	0.0010	0.0044	0.0000	31.1	1.0	28.5	0.3
DC0921-1													
DC0921-1-01	552	12910	0.04	0.0493	0.0012	0.0265	0.0009	0.0038	0.0000	26.6	0.9	24.6	0.3
DC0921-1-02	548	11648	0.05	0.0496	0.0010	0.0256	0.0006	0.0037	0.0000	25.6	0.5	24.0	0.2
DC0921-1-06	1644	32095	0.05	0.0485	0.0010	0.0251	0.0005	0.0037	0.0000	25.1	0.5	24.0	0.2
DC0921-1-07	690	17027	0.04	0.0495	0.0009	0.0250	0.0005	0.0037	0.0000	25.1	0.5	23.5	0.1
DC0921-1-09	1629	33939	0.05	0.0479	0.0008	0.0247	0.0004	0.0037	0.0000	24.8	0.4	24.0	0.1
DC0921-1-10	1011	23862	0.04	0.0498	0.0009	0.0252	0.0005	0.0037	0.0000	25.3	0.5	23.6	0.1
DC0921-1-14	360	13566	0.03	0.0473	0.0008	0.0241	0.0004	0.0037	0.0000	24.2	0.4	23.8	0.1
DC0921-1-16	1244	23787	0.05	0.0470	0.0008	0.0243	0.0004	0.0037	0.0000	24.4	0.4	24.1	0.2
DC0921-1-17	461	15301	0.03	0.0494	0.0009	0.0255	0.0005	0.0037	0.0000	25.6	0.5	24.0	0.2
DC0921-1-18	873	22739	0.04	0.0473	0.0008	0.0241	0.0004	0.0037	0.0000	24.2	0.4	23.8	0.1
DC0921-1-19	904	24524	0.04	0.0486	0.0008	0.0245	0.0004	0.0036	0.0000	24.6	0.4	23.5	0.1
DC0921-1-20	400	13277	0.03	0.0483	0.0009	0.0247	0.0005	0.0037	0.0000	24.8	0.5	23.8	0.1
DC0925-1													
DC0925-1-01	687	1837	0.37	0.0469	0.0017	0.0298	0.0011	0.0046	0.0000	29.8	1.0	29.8	0.3
DC0925-1-02	1105	2849	0.39	0.0472	0.0013	0.0304	0.0008	0.0047	0.0000	30.4	0.8	30.0	0.2

DC0925-1-04	990	2049	0.48	0.0490	0.0019	0.0307	0.0011	0.0046	0.0000	30.7	1.1	29.4	0.3
DC0925-1-05	821	3250	0.25	0.0469	0.0014	0.0303	0.0009	0.0047	0.0000	30.3	0.9	30.1	0.3
DC0925-1-06	1479	2565	0.58	0.0473	0.0016	0.0296	0.0010	0.0045	0.0000	29.6	1.0	29.2	0.3
DC0925-1-07	995	2783	0.36	0.0484	0.0014	0.0313	0.0009	0.0047	0.0000	31.3	0.8	30.2	0.3
DC0925-1-08	492	1806	0.27	0.0482	0.0016	0.0304	0.0010	0.0046	0.0000	30.4	1.0	29.5	0.3
DC0925-1-09	975	3488	0.28	0.0486	0.0015	0.0303	0.0009	0.0045	0.0000	30.3	0.9	29.0	0.2
DC0925-1-13	223	856	0.26	0.0507	0.0029	0.0324	0.0018	0.0047	0.0001	32.4	1.8	30.1	0.4
DC0925-1-14	698	2329	0.30	0.0472	0.0015	0.0303	0.0010	0.0046	0.0000	30.3	1.0	29.9	0.2
DC0925-1-17	523	1762	0.30	0.0484	0.0018	0.0317	0.0011	0.0048	0.0000	31.7	1.1	30.6	0.3
DC0925-1-18	592	1971	0.30	0.0498	0.0018	0.0319	0.0011	0.0047	0.0000	31.9	1.1	30.1	0.3
DC0925-1-19	736	2085	0.35	0.0485	0.0017	0.0313	0.0011	0.0047	0.0000	31.3	1.1	30.1	0.2
DC0925-1-20	911	2990	0.30	0.0475	0.0016	0.0301	0.0010	0.0046	0.0000	30.1	1.0	29.6	0.2
DC0925-1-21	1075	4180	0.26	0.0498	0.0013	0.0322	0.0008	0.0047	0.0000	32.1	0.8	30.1	0.2
DC0925-1-22	625	2311	0.27	0.0466	0.0016	0.0302	0.0010	0.0047	0.0000	30.2	1.0	30.3	0.3
DC0925-1-23	2132	6008	0.35	0.0467	0.0010	0.0297	0.0006	0.0046	0.0000	29.7	0.6	29.6	0.2
DC0925-1-24	1069	3144	0.34	0.0492	0.0013	0.0315	0.0008	0.0047	0.0000	31.5	0.8	30.0	0.2
DC0916-4													
DC0916-4-01	965	3047	0.32	0.0469	0.0011	0.0304	0.0007	0.0047	0.0001	30.4	0.7	30.2	0.2
DC0916-4-04	599	1609	0.37	0.0472	0.0019	0.0305	0.0012	0.0047	0.0001	30.5	1.2	30.1	0.3
DC0916-4-06	1031	3040	0.34	0.0499	0.0016	0.0316	0.0010	0.0046	0.0001	31.6	1.0	29.6	0.2

DC0916-4-07	933	5317	0.18	0.0484	0.0013	0.0312	0.0008	0.0047	0.0001	31.2	0.8	30.1	0.2
DC0916-4-08	857	2623	0.33	0.0490	0.0016	0.0315	0.0010	0.0047	0.0001	31.5	1.0	30.1	0.2
DC0916-4-09	890	2572	0.35	0.0491	0.0016	0.0317	0.0010	0.0047	0.0001	31.7	1.0	30.1	0.2
DC0916-4-10	1420	3323	0.43	0.0485	0.0011	0.0314	0.0007	0.0047	0.0001	31.4	0.7	30.2	0.2
DC0916-4-11	1396	4405	0.32	0.0488	0.0013	0.0315	0.0009	0.0047	0.0001	31.5	0.8	30.1	0.2
DC0916-4-12	918	1903	0.48	0.0504	0.0016	0.0322	0.0010	0.0047	0.0001	32.2	1.0	30.0	0.2
DC0916-4-14	878	3069	0.29	0.0452	0.0012	0.0287	0.0008	0.0046	0.0001	28.7	0.8	29.6	0.2
DC0916-4-15	1967	3810	0.52	0.0468	0.0011	0.0301	0.0007	0.0047	0.0001	30.1	0.7	30.0	0.2
DC0916-4-16	887	2723	0.33	0.0453	0.0014	0.0293	0.0009	0.0047	0.0001	29.4	0.9	30.1	0.3
DC0916-4-17	526	1321	0.40	0.0487	0.0019	0.0313	0.0012	0.0047	0.0001	31.3	1.2	30.1	0.3
DC0916-4-18	550	1702	0.32	0.0466	0.0017	0.0303	0.0011	0.0047	0.0001	30.3	1.1	30.3	0.2
DC0916-4-19	853	3052	0.28	0.0467	0.0012	0.0305	0.0008	0.0047	0.0001	30.5	0.8	30.5	0.2
DC0916-4-20	760	1778	0.43	0.0521	0.0017	0.0346	0.0011	0.0048	0.0001	34.5	1.1	31.1	0.4
DC0916-4-21	678	2505	0.27	0.0481	0.0013	0.0310	0.0008	0.0047	0.0001	31.0	0.8	30.1	0.2
DC0916-4-22	986	1352	0.73	0.0537	0.0022	0.0346	0.0014	0.0047	0.0001	34.5	1.3	30.3	0.3
DC0909-3													
DC0909-3-03	821	1456	0.56	0.0482	0.0020	0.0309	0.0013	0.0047	0.0000	30.9	1.3	30.0	0.3
DC0909-3-06	550	9162	0.06	0.0465	0.0009	0.0309	0.0006	0.0048	0.0000	30.9	0.6	30.9	0.2
DC0909-3-08	410	1170	0.35	0.0491	0.0024	0.0315	0.0015	0.0047	0.0000	31.5	1.5	30.0	0.3
DC0909-3-09	687	10824	0.06	0.0466	0.0008	0.0301	0.0005	0.0047	0.0000	30.1	0.5	30.0	0.2

DC0909-3-11	2012	12759	0.16	0.0484	0.0009	0.0317	0.0007	0.0047	0.0001	31.7	0.7	30.4	0.4
DC0909-3-14	193	622	0.31	0.0492	0.0031	0.0314	0.0019	0.0047	0.0001	31.4	1.9	30.1	0.5
DC0909-3-15	261	1064	0.25	0.0514	0.0025	0.0338	0.0016	0.0048	0.0001	33.7	1.6	30.9	0.4
DC0909-3-16	122	4882	0.02	0.0480	0.0011	0.0320	0.0008	0.0048	0.0000	32.0	0.8	31.0	0.3
DC0909-3-18	1646	12295	0.13	0.0473	0.0008	0.0317	0.0006	0.0049	0.0000	31.7	0.6	31.2	0.3
DC0909-3-19	210	781	0.27	0.0502	0.0028	0.0319	0.0017	0.0047	0.0001	31.8	1.6	30.2	0.4
DC0909-3-20	387	1703	0.23	0.0503	0.0021	0.0337	0.0014	0.0049	0.0001	33.6	1.4	31.4	0.4
DC0909-3-22	30	1250	0.02	0.0487	0.0022	0.0315	0.0014	0.0048	0.0001	31.5	1.4	30.6	0.4

U contents of 856–6008 ppm. The weighted mean $^{206}Pb/^{238}U$ age of 29.79 ± 0.21 Ma (MSWD=2.9) should represent the age of crystallization (Figure 14e). Zircon grains from the sample DC0916-4 are euhedral shapes, with oscillatory zonings throughout the whole grains (Figure 14m). The grains have aspect ratios between 1:1 and 6:1, and lengths of ~400 μm. 18 laser spots were analyzed on the rims of oscillatory zonings. These data have Th contents of 526–1967 ppm, U contents of 1321–5317 ppm. The weighted mean $^{206}Pb/^{238}U$ age of 30.09 ± 0.13 Ma (MSWD=1.4) is interpreted to be the crystallization age for the rock (Figure 14f). Zircon grains from the sample DC0909-3 are euhedral shapes (Figure 14n). Most of the zircons have oscillatory zonings throughout the whole grains. A few zircons have inherited cores. Most of the rims are darker than the cores, indicative of high U content in the rims. The grains have aspect ratios between 1:1 and 5:1. 12 laser spots were analyzed on the rims of oscillatory zonings. These data have Th contents of 30–2012 ppm, U contents of 622–12759 ppm. The weighted mean $^{206}Pb/^{238}U$ age of 30.45 ± 0.33 Ma (MSWD=3.4) should represent the age of crystallization (Figure 14g).

Our present dating results show that the U-Pb zircon crystallization ages range from 23.2-30.5 Ma, falling in the range of 30–20 Ma (Cao et al., 2011a; Liu et al., 2020), reflecting the timing of shearing.

5 Discussion

5.1 Doming in Southeastern Tibet

5.1.1 Strike-slip shear zones vs. domes

The above discussions reveal that most of the highly sheared high-grade metamorphic rocks of Proterozoic protoliths are exposed along Cenozoic high strain zones in Southeastern

Tibet, e.g., the ASRR and GLG-SG belts. They have been widely regarded as the results of strike-slip shearing (Leloup et al., 1993, 2001; Tapponnier et al., 1990). Meanwhile, there are also some highly sheared high-grade metamorphic complexes in areas between these high strain zones, e.g., the Ximeng (Chen et al., 2017a), Doi Inthanon-Doi Suthep complex (Rhodes et al., 2000), and the Bu Khang complexes (Jolivet et al., 1999). Wherever located, they show marked similarities in structural characteristics, kinematics, and ages of exhumation, etc.

Interpretations of the tectonic evolution of the complexes exist in the last decades. Early and some recent discussions are mostly based on the traditional strike-slip shear zone model. For example, the middle to south segment of Ailao Shan complex, the south segment of Yao Shan complex, and the north segment of Diancang Shan complex (Figures 15a-15c) were interpreted as parts of large-scale strike-slip shear zone, due to the lack of the limb of the antiformal structures. Domal configurations in the Xuelong Shan, DNCV are attributed to the results of strike-slip shearing (Anczkiewicz et al., 2007; Zhang et al., 2014).

Our present structural analysis of the complexes indicates that the regional structural styles of the metamorphic complexes are dominated by domal patterns (Figure 15). They are either short-axis or linear domes. Domes in the plate interior have preserved their intact domal structural pattern. For example, the Ximeng complex is characterized by an oval-shaped surface pattern that has long axes paralleling to NNW-SSE (Figure 15d). Others, especially those along the high strain zones, were destructed by late faulting. In this case, only one limb of the domes is preserved (Figures 15a-15c). One (e.g., Diancang Shan and Ailao Shan) or both (e.g., Yao Shan) limbs were cut by Holocene faults. The domes thus exhibit monoclinal structures in which foliations at different parts dip in the same direction. However, original hinge zones of the domes are preserved, e.g., at the northern segments of Ailao Shan and northern end of the Yao Shan complexes, foliations and lineations of folded mylonitic rocks dip and plunge to NW (Figures 15b and 15c). At the southern slope of the Diancang Shan complex, foliations and lineations mainly dip and plunge to S (Figure 15a).

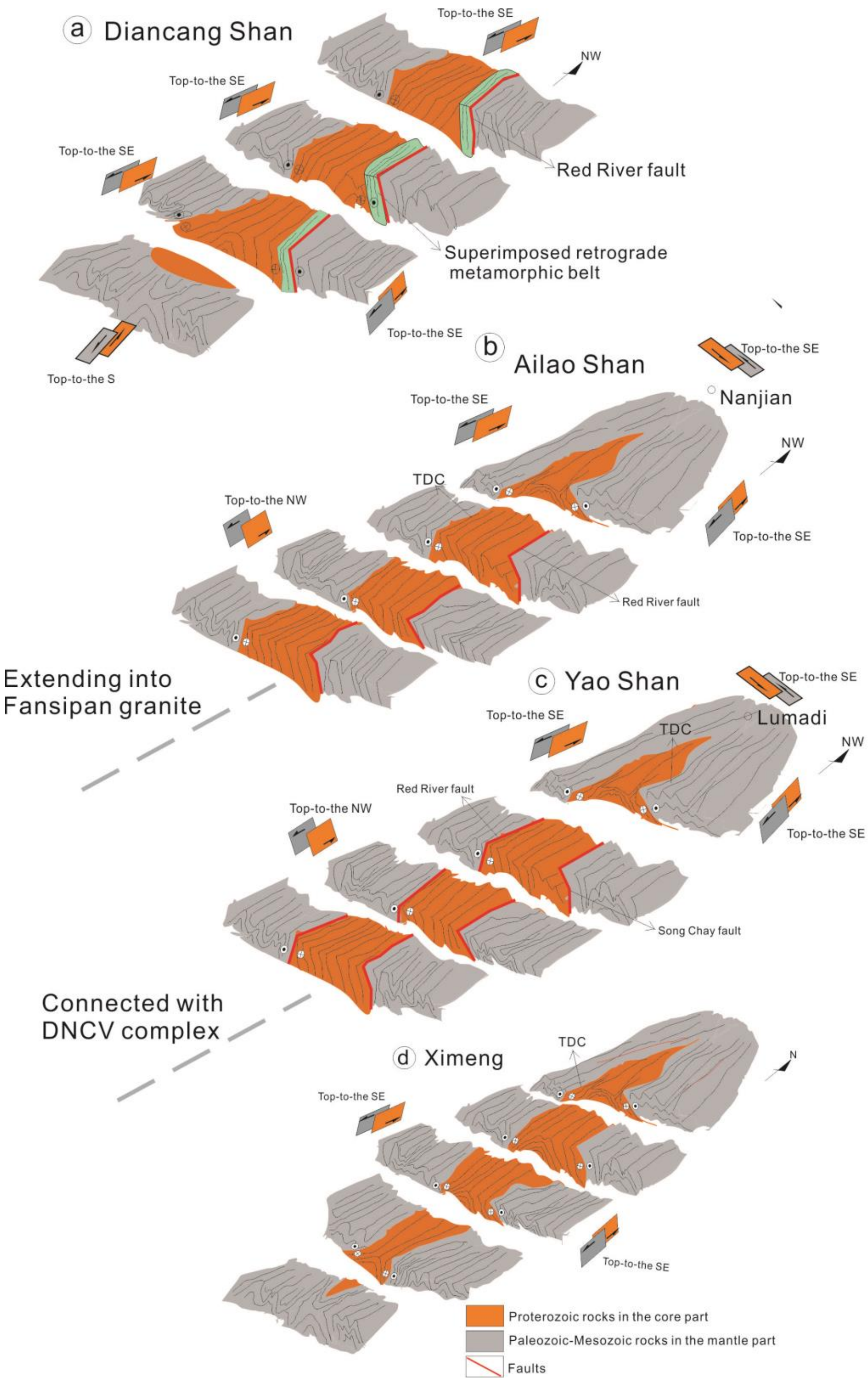

Figure 15. Sketch cartoons showing the structural configurations and geometries of the representative complexes in Southeastern Tibetan Plateau.

5.1.2 Kinematics during doming

In the study of Xuelong Shan complex, Zhang et al. (2014) suggested doming under the framework of regional left-lateral strike-slip shearing. In such a case, the core part on the east side moves southeastward, whereas on the west side it moves northwestward. This pattern of movement would lead to two sides of the core part move in the opposite direction, breaking the core part of the dome structure. The same situation in the study of Day Nui Con Voi dome (Anczkiewicz et al., 2007), which is suggested that left-lateral shearing in the two limbs, and the two sides of core part move in different directions. Although dome structures were proposed in these two studies, evolution models are still based on left-lateral shearing.

Structural measurements reveal the general parallelism between the long axes (or hinges) of the dome structures, and the stretching lineations and hinges of outcrop-scale A-type folds at different parts of the domes, which may suggest that the dome structures are of A-type domes. It is also shown that there are long limbs that strike in the orientation of the lineations and short hinge zones occur at both ends of the domes. Consequently, the kinematics of shearing during doming vary significantly from place to place. Based on structural framework and kinematic analyses, in the domes with two limbs dipping oppositely, e.g., the northern segments of the Ailao Shan and Yao Shan complexes, the southern part of Diancang Shan, and Ximeng complexes, the northeastern and southwestern limbs are dominated by right-lateral and left-lateral shearing, respectively (Figure 15). Shear sense indicators are compatible, in both limbs, with a core-to-the NW movement (Figure 15). It is noteworthy that in the southern slopes of the Diancang Shan and Ximeng complexes, the foliations dip to south, and possess shear sense of top-to-the S shearing or normal slipping (Figures 15a and 15d). In the southern segment of Ailao Shan, most of the foliations dip to NE, and are characterized by left-lateral shear, which reflect the core part moving NW relative to the mantle part (Figure 15b). The southwestern limb of the dome is well preserved, whereas the northeastern limb is truncated by the Red River fault. Similarly, the southern Yao Shan complex has the same structural configuration as that of the southern Ailao Shan complex, whereas the northeastern limb of the Yao Shan complex was cut by the Song Chay fault (Figure 15c).

In recent years, some studies have also shown the presences of right-lateral shear indicators along the ASRR belt (Chen et al., 2016; Zhang et al., 2014; Zhou et al., 2002), which challenged the traditional concept of ASRR shear zone as a left-lateral strike-slip shear zone. About the appearance of right-lateral shear indicators along the shear zone and the fact of core parts move towards NW relative to the mantle part, one assumption is that subhorizontal detachment movement occurred towards SE firstly (Figure 16a), and subsequently superimposed by folding during subsequent deformation (Figure 16b). Although this pattern would allow opposite shear indicators to exist in the opposite dipping limbs (Figure 16b) and the core part moves to NW relative to the mantle part, but the stretching lineation should be consistent with the superimposed fold axes in order to meet the facts of widely development of A-type folds in southeastern Tibet. Another assumption is that two opposite dipping normal faults developed along both flanks of the belt. It should keep their strikes be highly consistent with the regional stretching lineations (Figure 16c). Meanwhile, for middle and lower crustal rocks to be exhumated to near surface, the two normal faults should be rooted deeply in the crust. These two assumptions seem to be difficult to be satisfied in the nature. Therefore, only the core rocks move or flow relative to the mantle rocks towards NW with progressive shearing deformation that can meet contrast kinematics in two limbs and consistent movement for the core parts, i.e., core parts move towards NW relative to the mantle part (Figure 16d).

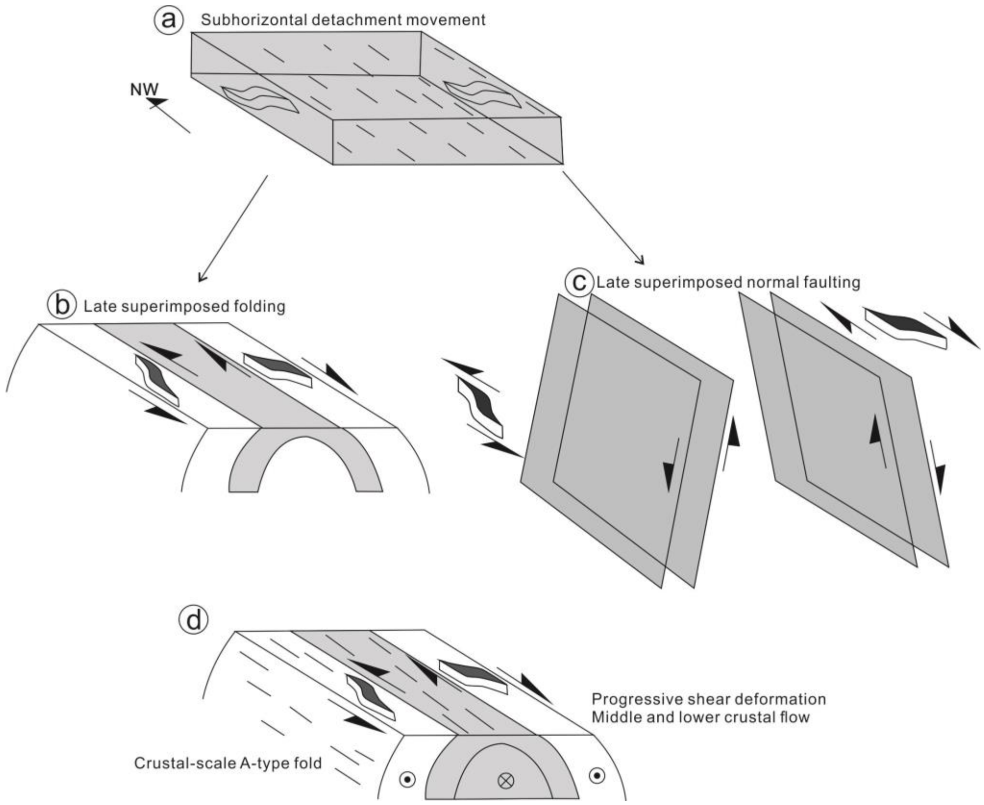

Figure 16. Possible models for opposite kinematics existing in two limbs. Subhorizontal detachment movement firstly occurred (a), then superimposed by late folding (b) and faulting (c), resulting in opposite kinematics in the two limbs. d: Middle and lower crustal flow accompanied by progressive shear deformation results in opposite kinematics in the two limbs and crustal-scale A-type fold.

5.1.3 Two-layer structure of the domes

In the domes, highly sheared Proterozoic high-grade metamorphic rocks constitute the core parts which are mantled by sheared Paleozoic-Mesozoic low-grade metamorphic rocks. The metamorphic assemblages and deformation microstructures of different parts of the domes obviously change with stratigraphic horizons (Figure 17). The lower the rocks in the stratigraphic horizons are, the higher their metamorphic and deformation temperatures are. At the same time, the formation of dome structures is related to progressive shearing, from analyses of deformation structures and fabric characteristics of each part of the dome structures.

Thus the rocks are characterized by rheological stratification during shearing: the core parts are characterized by high-grade metamorphism (high amphibolite facies) and high-temperature deformation (500~600℃) with locally superimposed lower temperature deformation (~300℃) in the later stage during progressive shearing, while the mantle parts are characterized by low-grade metamorphic rocks (green schist facies) and low-temperature deformation (~300℃) (Figure 17) and superimposed by much lower temperature deformation. Contrasting metamorphic grades and deformation temperatures, and identical structural elements (foliations, lineations, and shear senses) and kinematics exist between the core and mantle parts. Such changes are related to the occurrence of shear discontinuities (TDC, Chen et al., 2016) during doming of the complexes (e.g., Diancang Shan, Ailao Shan, Yao Shan-Day Nui Con Voi and Ximeng, Figure 17).

788

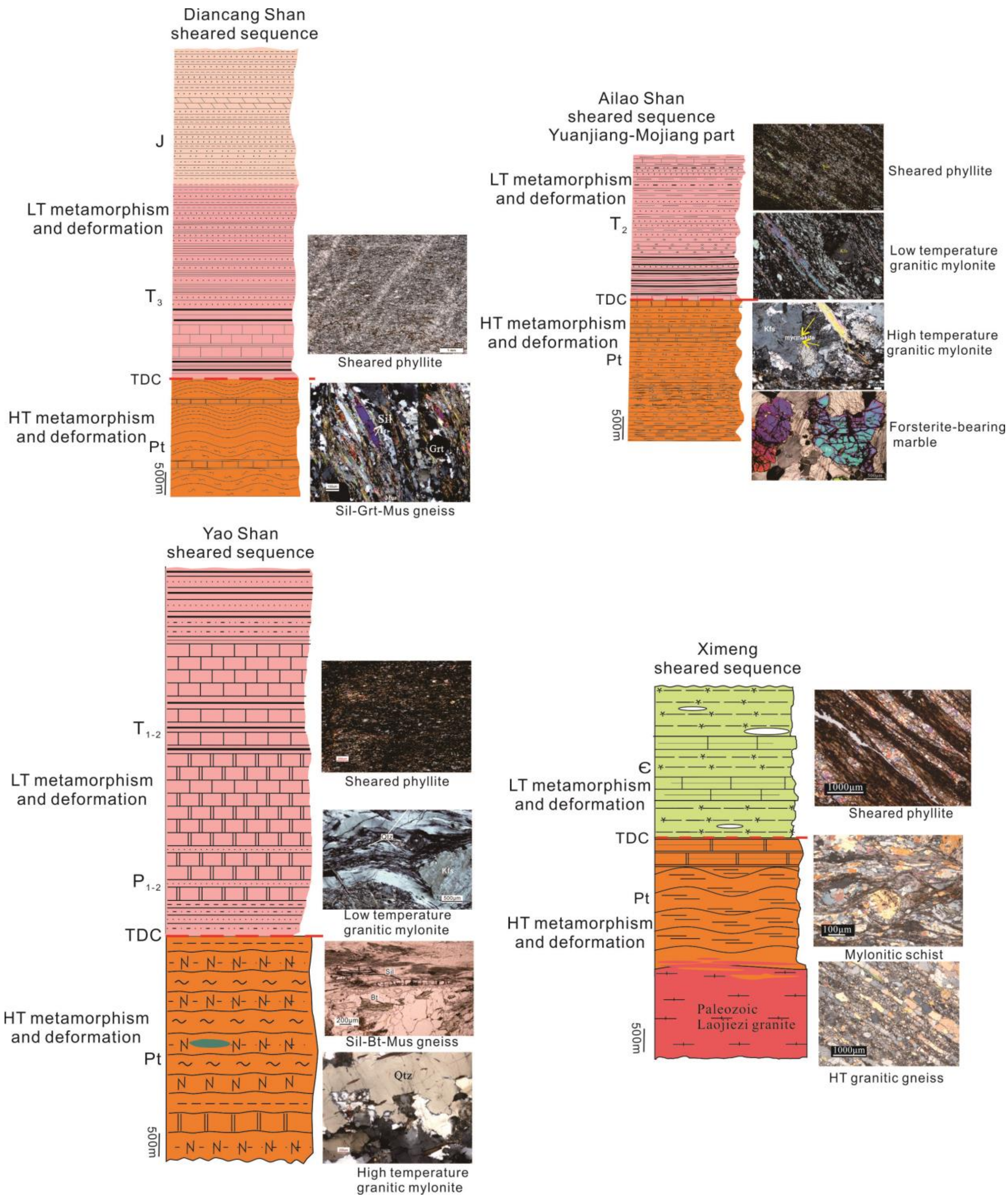

789 **Figure 17.** Stratigraphic columns of the Diancang Shan, Ailao Shan, Yao Shan and Ximeng complexes
790 showing the existence of a tectonic discontinuity (TDC) between the core and mantle parts. Representative
791 micro photos were shown for the metamorphic and deformation temperature of the core and mantle parts.

5.2 Thermal evolution and exhumation of the domes in southeastern Tibet since Oligocene

The timing of shearing and exhumation of the metamorphic complexes has long been the subject of extensive studies in the last decades. Early studies reported crystallization ages of syn-kinematic magmatic minerals (zircon U-Pb; Leloup et al., 1995), metamorphic minerals (monazite Th-Pb; Gilley et al., 2003), and cooling ages of potassium-bearing minerals (Ar-Ar; Harrison et al., 1996) as old as 35 Ma, arguing for an early initiation of shearing along the ASRR tectonic belt at 35 Ma. However, recent studies (Cao et al., 2011a; Liu et al., 2020; Searle et al., 2010; Tang et al., 2013) reveal the existence of pre-, syn-, and post- kinematic dikes (Figure 18b). Pre-kinematic high-potassium alkaline magmatism was active from ca. 41 Ma (or older) to 30 Ma possibly due to removal of thickened lithosphere around eastern Tibet (Chuang et al., 1997; Liu et al., 2020; Wang et al., 1998). The processes might have been associated with a significant perturbation of geothermal structure in the lithosphere owing to replacement of the basal lithospheric mantle by a hotter and lighter asthenosphere (Platt & England, 1993; Wang et al., 1998). The event is consistent with an Eocene amphibolite- to granulite-facies peak metamorphism and formation of anatectic melts along the ASRRB (Leloup & Kienast, 1993). Shearing along the ASRRB occurred between ca. 30 and 23–20 Ma (Figure 18b, Cao et al., 2011a; Liu et al., 2020), accompanied by retrogressive metamorphism, partial melting, formation of granitic leucosomes, and cooling of the metamorphic rocks. As to the GLG belt, delamination of lower lithosphere around 30–26 Ma in southern Tibet allowed further underthrusting and indentation of the NE corner of Indian plate, triggering the development of a N-S–striking subvertical dextral shearing (Chiu et al., 2018), leading to exhumation of the Gaoligong complex and doming around it.

The closure temperature of U-Pb system is much higher than that of Ar/Ar dating system, which is very important to restrict the crystallization age or lower limit age of exhuming rock masses. It can provide not only the exact timing of deformation, but also the initial timing of thermal evolution. According to the thermochronological data from the previous studies (Cao et al., 2011b; Chen et al., 2015; Harrison et al., 1992, 1996; Leloup et al., 1993; Wang et al., 1998), the thermal and exhumation histories of the domes along the boundaries and the interior of the Sundaland block could be well recognized (Figures 18a and 18c). The Diancang Shan complex along the Ailao Shan belt has undergone two stages of cooling and exhumation (Figure 18c, Cao et al., 2011b) during 28-13 Ma and 5-0 Ma, respectively. The first stage is relatively slow with cooling rates of 11-21° C /Ma, while the second stage is relatively fast (concentrated between 45-50 ° C /Ma). The Ailao Shan complex has also two-stage cooling history since 35Ma, an early rapid cooling (44.80-714.29 ° C/Myr) and a late slow cooling (10.00-17.79 °C/Myr). The cooling paths are significantly different from that of Diancang Shan (Figure 18c, Chen et al., 2015). The transition from rapid cooling in the early stage to slow cooling in the late stage occurred at a temperature of about 300° C along the whole Ailao Shan massif. In the direction of crossing the complex, the complex is uniformly uplifted and exhumed. However, along the strike of the complex, the Ar-Ar ages of amphibole and biotite gradually become younger from south to north, indicating that the early cooling stage is characterized by diachronous exhumation from southeast to northwest. However, there is no regular change in the late cooling stage, which is a slow, stable, and overall uplifting process from south to north (Chen et al., 2015). It is worthy suggesting that the cooling of the southern end of Ailao Shan complex since 35 Ma may be related to the intrusion and cooling of FanSiPan magma, while the rapid cooling from 30-23 Ma may be related to the ductile shear deformation accompanying doming and exhumation. In early studies, Leloup et al. (2001) obtained the cooling path of the Xuelong Shan complex (Figure 18c) on basis of thermochronology data. It is shown that the complex experienced rapid cooling and exhumation from 33-26 Ma. The cooling was suggested to be directly related to regional transpression. Furthermore, the Day Nui Con Voi complex has also experienced two-stage cooling since 34 Ma, slow cooling from 34 to 25 Ma and rapid cooling from 25 to 21 Ma (Figure 18c, Wang et al., 1998). The former is possibly related to geothermal perturbation caused by potassic magmatism (Chung et al., 1997), while the latter is ascribed to exhumation and uplift caused by shearing (Wang et al., 1998). Within the Sundaland block, the Ximeng complex has also undergone two stages of cooling since ca. 23 Ma (Figure 18c). The complex underwent a rapid cooling and exhumation process (112.6-648.1°C/Myr) between 22.93 Ma and 20.57 Ma in the early stage, followed by a slow exhumation process (7.5-16.9°C/Myr) in the late stage. The rapid exhumation process in the early stage is attributed to shearing accompanied by doming, while the slow exhumation in the late stage is resulted from overall slow exhumation during erosion process (Chen et al., 2017a). In addition, the thermal history of the Gaoligong complex started cooling from ca. 34 Ma, with a rapid cooling followed by a slow exhumation process (Figure 18c, Chiu et al., 2018).

The above results and analysis show that some of the domes possess early cooling since ca. 35 Ma probably due to significant perturbation of geothermal structure caused by widely developed high-potassium alkaline magmatism (Figure 18b, Chung et al., 1997, Liu et al., 2020), e.g., Xuelong Shan, Ailao Shan and Gaoligong Shan. However, most of the complexes in SE Tibet began to be exhumed since 30 Ma, according to the shearing timing constrained by syn-kinematic dykes (Figures 18a and 18b), while the initiation time is inconsistent at different places and mostly through two-stage cooling histories (Figure 18c). The initiation time of the Ximeng and

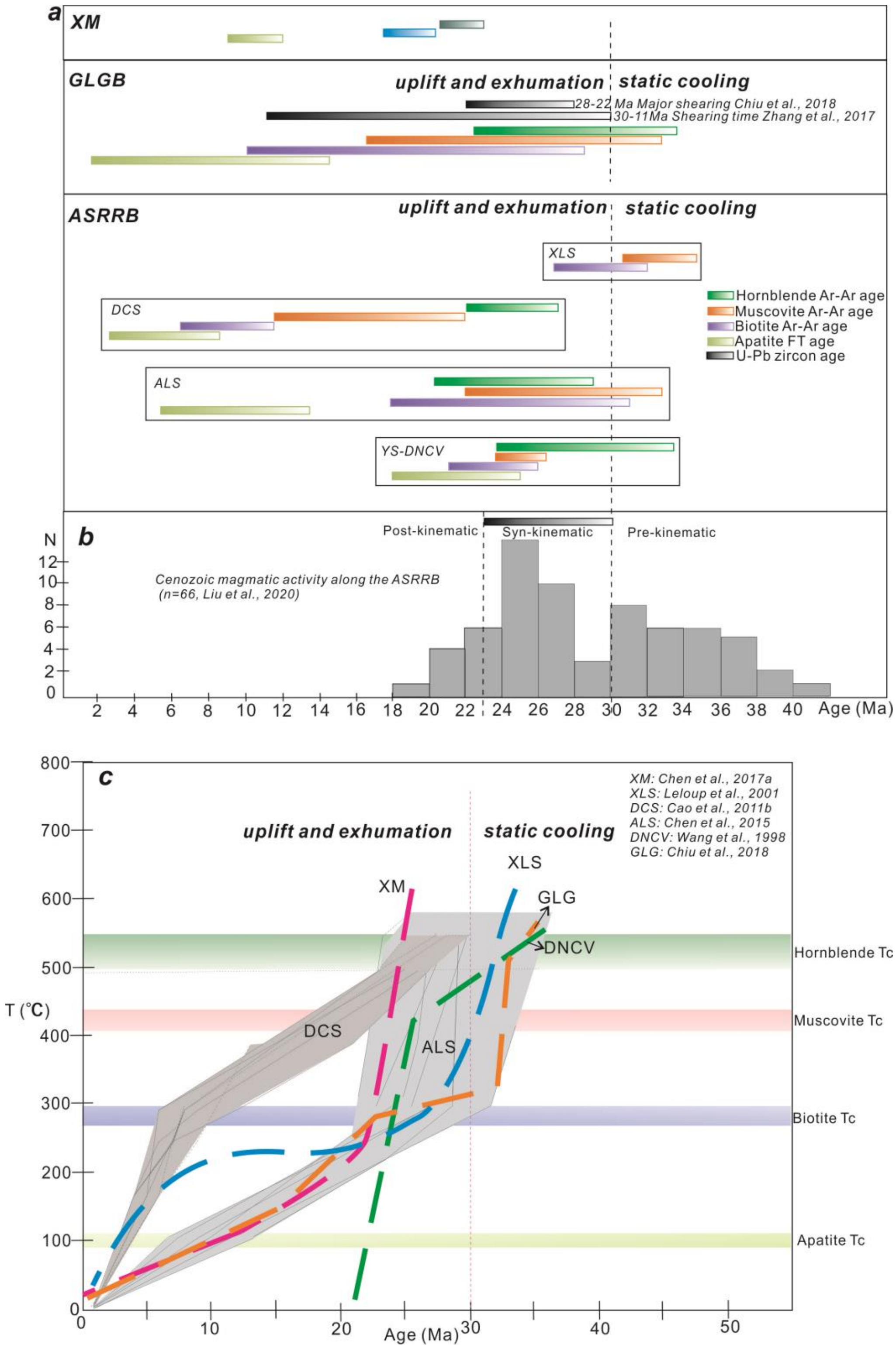

Figure 18. a: Ar-Ar ages and U-Pb ages of the complexes in SE Tibetan Plateau show the processes of static cooling and uplift cooling. b: Timing of Cenozoic magmatic activity along the Ailao Shan–Red River belt (modified after Liu et al., 2020). c: Cooling paths of these complexes.

Diancang Shan complexes is a little late, at about 25Ma (Figures 18a and 18c). On the other hand, Diancang Shan, Ailao Shan and DNCV complexes were exhumed diachronously from south to north (Cao et al., 2011b; Harrison et al., 1996; Leloup et al., 1993; Wang et al., 1998), which is not able to be applied to other complexes. Along the ASRR belt, the cooling paths and exhumation processes of Xuelong Shan, Diancang Shan, Ailao Shan, and DNCV have significantly different thermal evolutions and exhumation histories (Figure 18c), although they are located along the same tectonic belt. The different thermal histories suggest that the complexes are isolated units during Oligocene to Miocene crustal deformation in Southeast Tibet. According to the structural characteristics of the typical complexes mentioned above, the exhumation of the complexes is related to doming caused by middle and lower crust flow.

5.3 Mechanism of doming and tectonic implications

5.3.1 Mechanism of doming

Studies on exhumation of the metamorphic rocks, especially along the three major high strain zones, have been dominantly based on the tectonic extrusion model, in which the high strain zones are the boundary faults during the Cenozoic tectonic extrusion of the Sundaland block. For example, the exhumation of the high-grade metamorphic rocks in the Ailao Shan complex has traditionally been attributed to left-lateral strike shearing (Leloup et al., 1993; Harrison et al., 1997). As a result, transtension (e.g., Briais et al., 1993; Cao et al., 2011b; Harrison et al., 1996; Jolivet et al., 1999; Lee & Watkins, 1998; Liu et al., 2007) or transpression (e.g, Leloup et al., 2001; Schoenbohm et al., 2004; Wang & Burchfiel, 1997;

Zhang et al., 2010, 2017) along the boundary high strain zones are believed to be the main driving forces for exhumation. The "zipper" mode under transtension setting was proposed and applied to DNCV complex and Ailao Shan complex (Harrison et al., 1996; Leloup et al., 2001) and Mogok complex (Bertrand et al., 2001), in which diachronous shearing was suggested to be responsible for the initiation of strike-slip shear zones like the opening of zippers. Liu et al. (2007) emphasized that the SE Tibet was in an extensional area due to differential rotation between the Indochina block and the India plate since 33 Ma. The tectonic extension resulted in the formation of many metamorphic core complexes (e.g., the Diancang Shan, Liu et al., 2007). Anczkiewicz et al. (2002) put forward that under northeast - southwest extension, the subvertical fault suffered from progressive expansion, and the space has been injected by high amphibolite facies middle-lower crustal rocks, causing the formation and exhumation of gneiss dome. Jolivet et al. (2001) proposed that there exists a subhorizontal shear zone in the middle crust, in which the bottom of the Song Chay fault is developed. Transtension along the Song Chay fault led to exhumation of DNCV complex, while the adjacent Bu Khang dome was formed under a pure extensional background. Searle et al. (2010) stressed the importance of transpression on complex exhumation, and argued that rocks could not be exhumed by extension or transtension without a driving force from the bottom of the complex, and that the high-grade metamorphic rocks in the complex are uplifting Indosinian rocks. Cao et al. (2011b) conducted a detailed study on the exhumation of Diancang Shan dome and suggested that the slow exhumation process was caused by left-lateral shear during late Oligocene to Miocene, and rapid exhumation was resulted from brittle-ductile normal fault in late Miocene and brittle fault from early Eocene to Holocene. Zhang et al. (2014), in recent studies of the Xuelong Shan complex, proposed that compression resulted in the formation of a regional gneisses dome. Xu et al. (2015) considered that horizontal detachment system and right-lateral slip shear were the main forces for exhumation of the Gaoligong gneiss dome.

Comprehensive structural and thermo-chronological analyses of these metamorphic complexes provide new constraints on exhumation mechanisms and dynamics for the formation of the metamorphic domes in SE Tibetan plateau. By studying the structural characteristics of the metamorphic complexes, it is shown that the core parts move towards NW or NNW direction relative to the mantle parts during anticlinal doming. The orientations of the hinges of the domes are consistent with those of the stretching lineations, suggesting that these complexes are crustal-scale A type folds (Figure 15). The consistency and simultaneity between the regional stretching lineations and fold hinges indicate that the formation of A type folds was related to the northwestward movement of the middle and lower crust relative to the upper crust. In the process of folding (doming) and progressive shearing, the rocks located in the lower lithostratigraphic level (core part) experienced medium to high temperature deformation and metamorphism, while the rocks located in the upper lithostratigraphic level (mantle part) experienced low-temperature deformation and metamorphism. Accompanying the progressive shearing and exhumation, the early medium to high temperature deformation is partly superimposed by subsequent low temperature deformation. Such a process resulted from middle and lower crustal flow, in which crustal rocks are dominated by tangential (or subhorizontal) shear movement (Figure 19a). Although the vertical component is small, the rocks in the deep level can be exhumed in areas with the most intensive lateral flow (such as the ASRR tectonic belt, GLG-SG tectonic belt) due to large scale displacement (Leloup et al., 1995). Shear discontinuities were induced in the process of uplifting of the core rocks, resulted in cut-off or thinning of shallow strata at different locations, and made the deformed core rocks to be in direct contact with different shallow strata due to the vertical shear component (Figure 19b). The shearing was accompanied by regional folding (doming) during progressive deformation that contributed to simultaneous exhumation of the rocks in the core and mantle parts (Figure 19b).

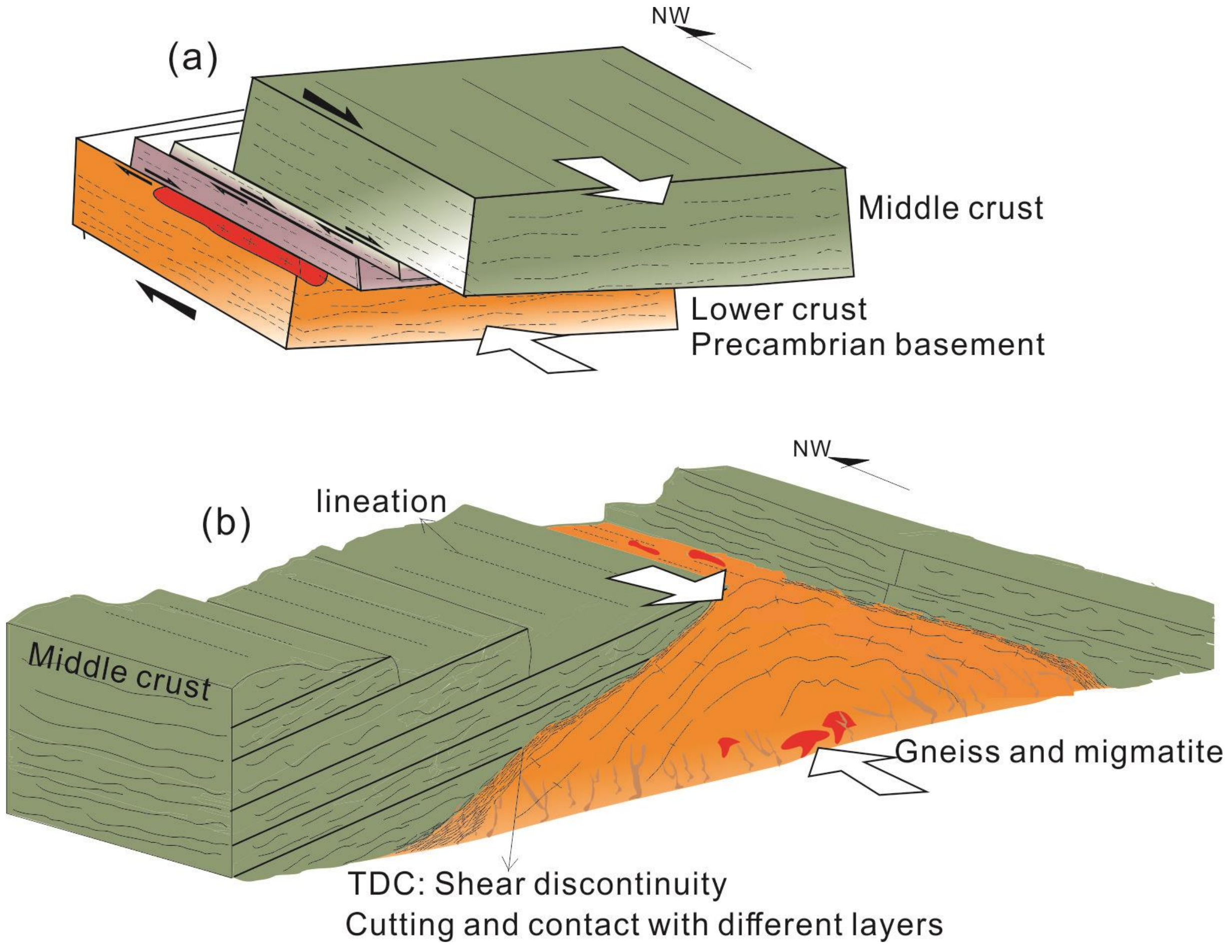

Figure 19. Evolution model of the A-type dome structure. (a) Tangential ductile shearing in the early stage. (b) With progressive shearing of lateral flow, shear discontinuities were induced resulted in cut-off or thinning of shallow strata, and made the deformed core rocks to be in direct contact with the shallow level strata, which is accompanied by regional folding and exhumation.

5.3.2 Implications for intraplate deformation

It is shown from the present study that the metamorphic complexes in SE Tibetan plateau suffered from ductile shear deformation accompanied by regional folding (doming) since Oligocene, whether they are distributed in the eastern ASRR belt: Xuelong Shan, Diancang

Shan, Ailao Shan and Yaoshan -DNCV complexes, or the western GLG-SG belt: Gaoligong and Mogok complexes, or within the Sundaland block: Ximeng complex, Analyses of the deformation and exhumation characteristics suggest that deformation is not only limited along the boundary high strain zones, but distributed in the interior plate (Figure 20). The results highlight the importance of intraplate deformation of the Sundaland block. It is also shown that both intraplate deformation (Ximeng) and strain localization along boundary high strain zones are related to the middle-lower crust flow during the lateral extrusion of the block.

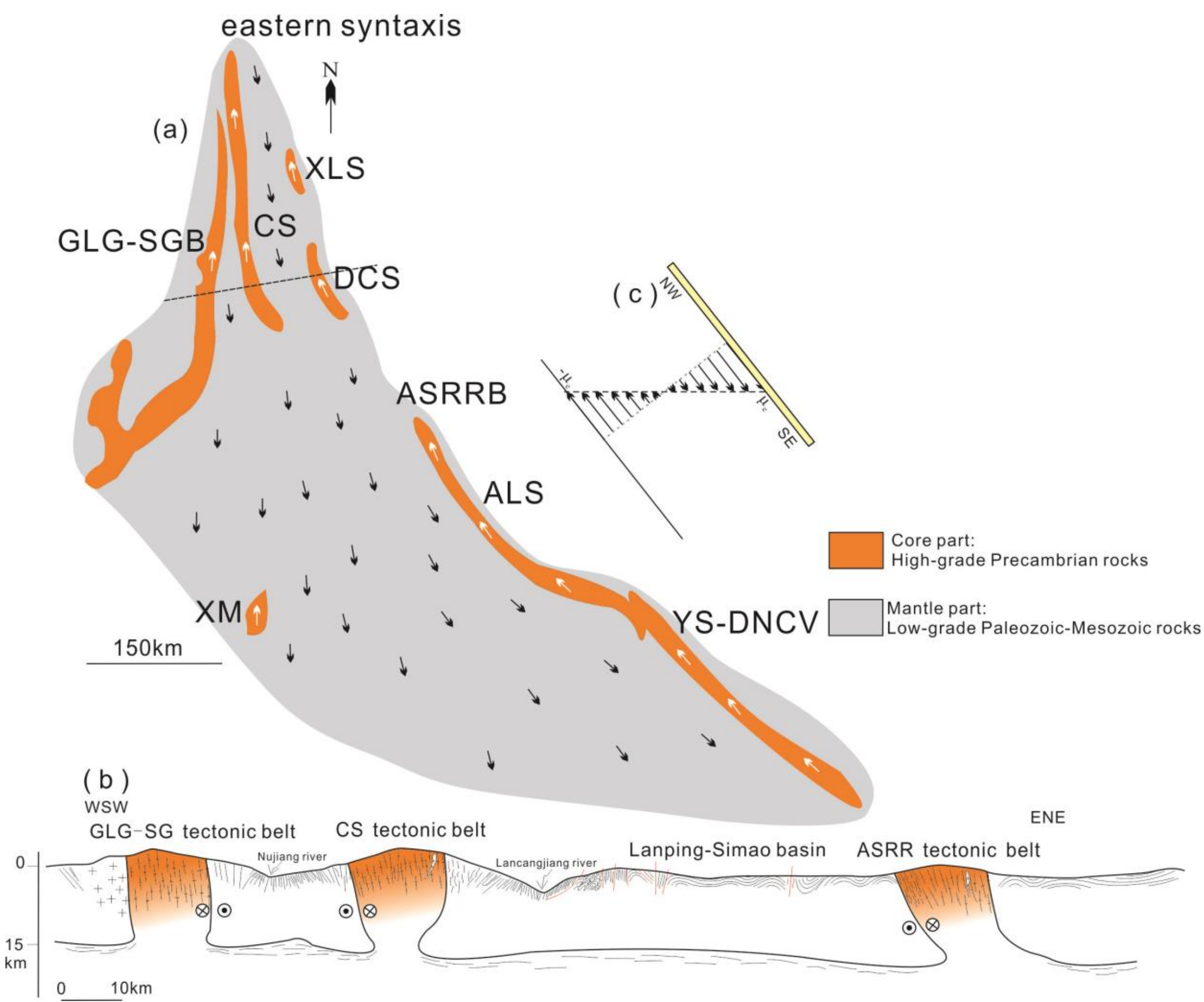

Figure 20. Schematic diagrams showing the middle-lower crustal flow and strain localization belts. The white and black arrows indicate the movement of the mantle and core parts, respectively. (a) Planar graph of the metamorphic complexes and the flow pattern; (b) Schematic profile shows the middle-lower crustal flow along

the three high strain zones; (c) Couette flow of crustal mass shows the southward flow of the rigid upper crust and northward flow of the viscous lower crust relative to the middle-upper crust. For the abbreviations, refer to figure caption 1.

On one hand, kinematic analysis reveals that the high-grade metamorphic rocks or the present core parts tend to flow NW relative to the low-grade metamorphic rocks or the present mantle parts during middle and lower crustal flow (Figure 20). There are three possible explanations for such a scenario (Chen et al., 2020). A first approach is that the crustal flow was driven by the northward subhorizontal flow with a downward positive velocity gradient. The other possibility is the southward moving of middle-upper crust and has a downward negative velocity gradient due to gravitational collapse of the plateau. One alternative and most probable explanation is the effect of a counter flow of southward flow of the rigid upper crust and northward flow of the viscous lower crust relative to the middle-upper crust, which also results in core-to-the north tangential shearing (Figure 20c). The former was driven by gravitational collapse of the plateau, whereas the latter by an unknown force which needs to further study. In such a case, the crustal flow follows the Couette flow, but the lower crustal masses relatively flow into the plateau (Chen et al., 2020).

On the other hand, differences exist in the pattern of middle and lower crustal flow. The Ailao Shan-Red River, Gaoligong-Sagaing and Chong Shan tectonic belts are characterized by channeled middle to lower crustal flow (Figure 20). However, flow in the interior plate may be distributed subhorizontal flow (e.g., Ximeng, etc.) as also proposed by Jolivet et al. (1999) in the study of Bukhang dome. In both cases, middle and lower crustal flow resulted in lateral crustal flow and vertical exhumation of the crustal masses, absorbing a large amount of deformation caused by India-Eurasia collision.

6 Conclusions

1. Structural analysis of the Diancang Shan, Ailao Shan, Yao Shan, Xuelong Shan, Ximeng and Gaoligong metamorphic complexes reveal that dome structures are widely developed in the southeastern Tibetan Plateau. The core parts are composed of high-grade metamorphic and high temperature deformed rocks which is partially superimposed by late low temperature deformation. While the mantle parts are characterized by low grade metamorphic rocks and low temperature deformation. In most cases, shear discontinuity exists between the core and mantle parts.
2. Most of the metamorphic complexes in SE Tibet began to be exhumed since 30 Ma, while their initiation was diachronous at different places and mostly through two-stage cooling histories. Formation and exhumation of the dome structures in southeastern Tibetan Plateau are related to the middle and lower crustal flow, during which shearing, folding and exhumation are simultaneous.
3. In the process of lateral escape of Sundaland block, middle and lower crustal flow resulted in lateral crustal flow and vertical exhumation of the crustal masses, absorbing a large amount of deformation caused by India-Eurasia collision. The deformation is not only confined to the edges of the block.

Acknowledgments, and Data

This study was financially supported by the National Natural Science Foundation of China (Grant No. 41902203 and 91955205) and and the Fundamental Research Funds for the Central Universities (Grant No. 2652018114). The data from the present study can be found at https://figshare.com/s/222a7ce046a6612147d3

References

Anczkiewicz, R., Viola, G., Müntener, O, Thirlwall, M. F., Villa, I. M., & Quong, N. Q. (2007). Structure and shearing conditions in the Day Nui Con Voi massif: Implications for the evolution of the Red River shear zone in northern Vietnam. *Tectonics*, 26(2), 344-346

Armijo, R., Tapponnier, P., & Han, T. (1989). Late Cenozoic right-lateral strike-slip faulting in southern Tibet. *Journal of Geophysical Research Solid Earth*, 94(B3), 2787-2838.

Bai, D. H., Unsworth, M. J., Meju, M. A., Ma, X. B., Teng, J. W., Kong, X. R., et al. (2010). Crustal deformation of the eastern Tibetan Plateau revealed by magnetotelluric imaging. *Nature Geoscience*, 3(5), 358-362.

Beaumont, C., Jamieson, R. A., Nguyen, M. H., & Lee, B. (2001). Himalayan tectonics explained by extrusion of a low-viscosity crustal channel coupled to focused surface denudation. *Nature*, 414(6865), 738.

Bender, F., & Bannert, D. *Geology of Burma*, 1983.

Bergman, S. C., Leloup, P. H., Tapponnier, P., Scharer, U., & O'Sulliivan, P. (1997). Apatite fission track thermal history of the Ailao Shan-Red River shear zone, China. In: Paper Presented at Meeting, European Geosciences Union, Strasbourg, France, March, 23-27.

Bertrand G, Rangin C, Maluski H, & Bellon H. (2001). Diachronous cooling along the Mogok Metamorphic Belt (Shan scarp, Myanmar): the trace of the northward migration of the Indian syntaxis. *Journal of Asian Earth Sciences*, 19(5), 649-659.

BGMRYP (Bureau of Geology and Mineral Resources of Yunnan Province). (1990). Regional Geology of Yunnan Province. Geological Publishing House, Beijing (In Chinese with English abstract).

Briais, A., Patriat, P., & Tapponnier, P. (1993). Updated interpretation of magnetic anomalies and seafloor spreading stages in the South China Sea: implications for the Tertiary tectonics of Southeast Asia. *Journal of Geophysical Research*, 98, 6299– 6328

Burchfiel, B. C., Royden, L. H., Van der Hilst, R. D., Hager, B. H., Chen, Z., King, R. W., et al. (2008). A geological and geophysical context for the Wenchuan earthquake of 12 May 2008, Sichuan, People's Republic of China. *GSA Today*, 18(7), 4-11.

Cao, S. Y., Liu, J. L., Leiss, B., Neubauer, F., Genser, J., & Zhao, C. Q. (2011a). Oligo-Miocene shearing along the Ailao Shan–Red River shear zone: Constraints from structural analysis and zircon U/Pb geochronology of magmatic rocks in the Diancang Shan massif, SE Tibet, China. *Gondwana Research*, 19(4), 975–993. https://doi.org/10.1016/j.gr.2010.10.006

Cao, S. Y., Neubauer, F., Liu, J. L., Genser, J., & Leiss, B. (2011b). Exhumation of the Diancang Shan metamorphic complex along the Ailao Shan-Red River belt, southwestern Yunnan, China: Evidence from 40Ar/39Ar thermochronology. *Journal of Asian Earth Sciences*, 42, 525-550.

Cao, S. Y., Liu, J. L., & Leiss, B. (2010). Orientation-related deformation mechanisms of naturally deformed amphibole in amphibolite mylonites from the Diancang Shan, SW Yunnan, China. *Journal of structural geology*, 32(5), 606-622

Chen, X. Y., Liu, J. L., Burg, J. P., Tang, Y., Wu, W. B., & Yan, J. X. (2020). Structural evolution and exhumation of the Yulong dome: Constraints on middle crustal flow in southeastern Tibetan Plateau in response to the India-Eurasia collision. *Journal of Structural Geology*, 137, P104070 .

Chen, X.Y., Burg, J. P., Liu, J. L., Qi, Y. C., Fan, W. K., & Wang, K. (2019). Multistage remobilization of the Southwestern margin of the South China Plate: insights from zircon U-Pb geochronology and Hf isotope of granitic rocks from the Yao Shan complex, Southeastern Tibet Plateau. *Tectonics*, 38(2), 621-640.

Chen, X. Y., Liu, J. L., Qi, Y. C, Fan, W. K., Wang, K., Zhang, Y., & Chen, W. (2017a). Miocene structural evolution and exhumation of the Ximeng dome in Yunnan, southeastern Tibet: Implications for intraplate deformation during extrusion of the Sundaland block. *Journal of Asian Earth Sciences*, 141, 194-212.

Chen, X. Y., Liu, J. L., Fan, W. K., Qi, Y. C., Wang, W., Chen, J. F., & Burg, J. P. (2017b). Neoproterozoic granitoids along the Ailao Shan-Red River belt: Zircon U-Pb geochronology, Hf isotope analysis and tectonic implications. *Precambrian Research*, 299, 244–263. https://doi. org/10.1016/j.precamres.2017.06.024

Chen, X. Y., Liu, J. L., Weng, S. T., Kong, Y. L., Wu, W. B., Zhang, L. S., & Li, H. Y. (2016). Structural geometry and kinematics of the Ailao Shan shear zone: Insights from integrated structural, microstructural, and fabric studies of the Yao Shan complex, Yunnan, Southwest China. *International Geology Review*, 58(7), 849–873.

Chen, X. Y., Liu, J. L., Tang, Y., Song, Z. J., & Cao, S. Y. (2015). Contrasting exhumation histories along a crustal-scale strike-slip fault zone: The Eocene to Miocene Ailao Shan-Red River shear zone in southeastern Tibet. *Journal of Asian Earth Sciences*, 114, 174–187. https:// doi.org/10.1016/j.jseaes.2015.05.020

Chiu, Y. P., Yeh, M. W., Wu, K. H., Lee, T. Y., & Iizuka, Y. (2018). Transition from extrusion to flow tectonism around the eastern himalaya syntaxis. Geological Society of America Bulletin, 130(9-10).

Chung, S. L., Lee, T. Y., Lo, C. H., Wang, P. L., Chen, C. Y., Yem, N. T., et al. (1997). Intraplate extension prior to continental extrusion along the Ailao Shan-Red River shear zone. *Geology*, 25(4), 311–314. https://doi.org/10.1130/0091-7613(1997)0252.3. CO;2

Clark, M. K., & Royden, L. H., (2000). Topographic ooze: Building the eastern margin of Tibet by lower crustal flow. *Geology*, 28,703–706.

Clark, M. K., Bush, J. W. M., & Royden, L. H. (2005). Dynamic topography produced by lower crustal flow against rheological strength heterogeneities bordering the Tibetan Plateau. *Geophysical Journal International*, 162, 575–590.

Gilley, L., Harrison, T., Leloup, P. H., Ryerson, F., Lovera, O., & Wang, J. H. (2003). Direct dating of left-lateral deformation along the Red River shear zone, China and Vietnam. *Journal of Geophysical Research*, 108, 14-21.

Feng, Q. L., Chonglakmani, C. P., Helmcke, D., Ingavat-Helmckec, R., & Liu, B. P. (2005). Correlation of Triassic stratigraphy between the Simao and Lampang-Phrae Basins: implications for the tectonopaleogeography of Southeast Asia. *Journal of Asian Earth Sciences*, 24(6), 777-785.

Harrison, T. M., Chen, W., Leloup, P. H., Ryerson, F. J., & Tapponnier, P. (1992). An early Miocene transition in deformation regime within the Red River fault zone, Yunnan, and its significance for Indo-Asian tectonics. *Journal of Geophysical Research*, 97, 7159–7182.

Harrison, T. M., Leloup, P. H., Ryerson, F. J., Tapponnier, P., Lacassin, R., & Wenji, C. (1996). Diachronous initiation of transtension along the Ailao Shan–Red River shear zone, Yunnan and Vietnam, in Yin, A., and Harrison, T. M., eds., The tectonic evolution of Asia: New York, Cambridge University Press, 205–226.

Lacassin, R., Schärer, U., Leloup, P.H., Arnaud, N., Tapponnier, P., Liu, X.H., & Zhang, L.S. (1996). Tertiary deformation and metamorphism SE of Tibet: the folded tiger-leap décollement of NW Yunnan, china. *Tectonics*, 15, 605-622

Lee, G. H., & Watkins, J. S. (1998). Seismic sequence stratigraphy and hydrocarbon potential of the Phu Khanh Basin, offshore central Vietnam, South China Sea. *AAPG bulletin*, 82(9), 1711-1735.

Liu, Q. Y., Van Der Hilst, R. D., Li, Y., Yao, H. J., Chen, J. H., Guo, B., et al. (2014). Eastward expansion of the Tibetan Plateau by crustal flow and strain partitioning across faults. *Nature Geoscience*, 7(5), 361.

Metcalfe, I. (1996). Pre-Cretaceous evolution of SE Asian terranes. Geological Society, London, Special Publications, 106(1), 97-122.

Metcalfe, I. (2013). Gondwana dispersion and Asian accretion: Tectonic and palaeogeographic evolution of eastern Tethys. *Journal of Asian Earth Sciences*, 66, 1–33. https://doi.org/10.1016/j.jseaes.2012.12.020

Jian, P., Liu, D. Y., Kroner, A., Zhang, Q., Wang, Y. Z., Sun, X. M., & Zhang, W. (2009). Devonian to permian plate tectonic cycle of the paleo-tethys orogen in southwest china (i): geochemistry of ophiolites, arc/back-arc assemblages and within-plate igneous rocks - sciencedirect. *Lithos*, 113(3–4), 748-766.

Jolivet, L., Beyssac, O., Goffé, B., Avigad, D., Lepvrier, C., Maluski, H., & Thang, T. T. (2001). Oligo-Miocene midcrustal subhorizontal shear zone in Indochina. *Tectonics*, 20(1), 46–57. https://doi.org/10.1029/2000TC900021

Jolivet, L., Maluski, H., Beyssac, O., Goffé, B., Lepvrier, C., & Thi, P. T. (1999). Oligocene-Miocene Bu Khang extensional gneiss dome in Vietnam: Geodynamic implications. *Geology*, 27(1), 67–70. https://doi.org/10.1130/0091-7613(1999)0272.3.CO;2

Lee, H. Y., Chung, S. L., Wang, J. R., Wen, D. J., Lo, C. H., Yang, T. F., et al. (2003). Miocene Jiali faulting and its implication for Tibetan tectonic evolution. *Earth and Planetary Science Letters*, 205, 185-194.

Leloup, P. H., Arnaud, N., Lacassin, R., Kienast, J. R., Harrison, T. M., Trong, T. T. P., et al. (2001). New constraints on the structure, thermochronology and timing of the Ailao Shan–Red River shear zone, SE Asia. *Journal of Geophysical Research*, 106(B4), 6683–6732. https://doi.org/10.1029/2000JB900322

Leloup, P. H., Lacassin, R., Tapponnier, P., Schärer, U., Zhong, D., Liu, X., et al. (1995). The Ailao Shan-Red River shear zone (Yunnan, China), Tertiary transform boundary of Indochina. *Tectonophysics*, 251(1-4), 3–84. https://doi.org/10.1016/0040-1951(95)00070-4

Leloup, P. H., & Kienast, J. R. (1993). High-temperature metamorphism in a major strike-slip shear zone: The Ailao Shan–Red River, People's Republic of China. *Earth and Planetary Science Letters*, 118(1-4), 213–234. https://doi.org/10.1016/0012-821X(93)90169-A

Liang, H. Y., Campbell, I. H., Allen, C. M., Sun, W. D., Yu, H. X., Xie, Y. W., & Zhang, Y. Q. (2007). The age of the potassic alkaline igneous rocks along the Ailao Shan–Red River shear zone: Implications for the onset age of left-lateral shearing. *The Journal of Geology*, 115(2), 231–242. https://doi.org/10.1086/510801

Liu, J. L., Chen, X. Y., Tang, Y., Song, Z. J., & Wang, W. (2020). The Ailao Shan-Red River shear zone revisited: timing and tectonic implications. *Geological Society of America Bulletin*, 132, 1165-1182.

Liu, J. L., Tang, Y., Tran, M. D., Cao, S. Y., Zhao, L., Zhang, Z. C., et al. (2012). The nature of the Ailao Shan-Red River (ASRR) shear zone: Constraints from structural, microstructural and fabric analysis of metamorphic rocks from Diancang Shan, Ailao Shan and Day Nui Con Voi high grade massifs. *Journal of Asian Earth Sciences*, 47, 231–251. https://doi .org/10.1016/j.jseaes.2011.10.020.

Liu, J. L., Cao, S. Y., Zhai, Y. F., Song, Z. J., Wang, A. J., Xiu, Q. Y., et al. (2007). Rotation of crustal blocks as an explanation of Oligo-Miocene extension in Southeastern Tibet-evidenced by the Diancangshan and nearby metamorphic core complex. *Earth Science Frontiers*, 14(4), 40-48 (in Chinese with English abstract).

Molnar, P., & Tapponnier, P. (1975). Cenozoic tectonics of Asia: effects of a continental collision. *Science*, 280, 419- 426.

Morley, C. K. (2007). Variations in Late Cenozoic-Recent strike-slip and oblique extensional geometries, within Indochina: the influence of pre-existing fabrics. *Journal of Structural Geology*, 29, 36-58.

Morley, C. K. (2002). A tectonic model for the tertiary evolution of strike–slip faults and rift basins in SE Asia. *Tectonophysics*, 347(4), 189–215.

Nelson, K. D., Zhao, W., Brown, L. D., Kuo, J., Che, J, Lui, X., et al. (1996). Partially molten middle crust beneath southern Tibet: Synthesis of Project INDEPTH initial results. *Science*, 274, 1684–1688.

Peltzer, G., & Tapponnier, P. (1988). Formation and evolution of strike-slip faults, rifts, and basins during the India-Asia collision: An experimental approach. *Journal of Geophysical Research: Solid Earth*, 93(B12), 15085-15117.

Passchier, C. W., & Trouw, R. A. J. (2005). *Microtectonics* (p. 366). Berlin: Springer.

Platt, J. P., & England, P. C. (1993). Convective removal of lithosphere beneath mountain belts: Thermal and mechanical consequence. *American Journal of Science*, 293, 307–336.

Rippe, D., & Unsworth, M. (2010). Quantifying crustal flow in Tibet with magnetotelluric data. Phys. *Earth and Planetary Science Letters*, 179(3-4), 107-121.

Royden, L. H., Burchfiel, B. C., King, R. W., Wang, E. C., Chen, Z. L., Shen, F., & Liu, Y. P. (1997). Surface deformation and lower crustal flow in eastern Tibet. *Science*, 276, 788–790. https://doi.org/10.1126/ science.276.5313.788.

Schoenbohm, L. M., Whipple, K. X., Burchfiel, B. C., & Chen, L. (2004). Geomorphic constraints on surface uplift, exhumation, and plateau growth in the Red River region, Yunnan Province, China. *Geological Society of America Bulletin*, 116(7-8), 895-909.

Searle, M. P., Yeh, M.-W., Lin, T.-H., & Chung, S.-L. (2010). Structural constraints on the timing of left-lateral shear along the Red River shear zone in the Ailao Shan and Diancang Shan ranges, Yunnan, SW China. *Geosphere*, 6, 1–23.

Shen, F., Royden, L. H., & Burchfiel, B.C. (2001). Large-scale crustal deformation of the Tibetan Plateau. *Journal of Geophysical Research: Solid Earth*, 106(B4), 6793-6816.

Tapponnier, P., Lacassin, R., Leloup, P. H., Schärer, U., Dalai, Z., Haiwei, W., et al. (1990). The Ailao Shan/Red River metamorphic belt: Tertiary left lateral shear between lndochina and South China. *Nature*, 343(6257), 431–437. https://doi.org/10.1038/343431a0

Tapponnier, P., Peltzer, G., & Armijo, R. (1986). On the mechanics of the collision between India and Asia. Geological Society, London, Special Publications, 19(1), 113-157.

Tapponnier, P., Peltzer, G., Le Dain, A. Y., Armijo, R., & Cobbold, P. (1982). Propagating extrusion tectonics in Asia: new insights from simple experiments with plasticine. *Geology*, 10 (12), 611–616.

Tang, Y., Liu, J., Tran, M. D., Song, Z., Wu, W., Zhang, Z., et al. (2013). Timing of left-lateral shearing along the Ailao Shan-Red River shear zone: Constraints from zircon U–Pb ages from granitic rocks in the shear zone along the Ailao Shan Range, Western Yunnan, China. *International Journal of Earth Sciences*, 102(3), 605–626. https://doi.org/10.1007/s00531-012-0831-y

Wang, E., & Burchfiel, B. C. (1997). Interpretation of Cenozoic tectonics in the right lateral accommodation zone between the Ailao Shan shear zone and the eastern Himalayan syntaxis. *International Geology Review*, 39, 191–219.

Wang, P. L., Lo, C. H, Lee, T. Y., Chung, S. L., Lan, Y. C., & Yem, N. T. (1998). Thermochronological evidence for the movement of the Ailao Shan–Red River shear zone: a perspective from Vietnam. *Geology*, 26, 887–890.

Wu, W. B., Liu, J. L., Chen, X. Y., & Zhang, L. S. (2016). Zircon U-Pb ages, Hf isotope data, and tectonic implications of Early-Middle Triassic granitoids in the Ailaoshan high-grade metamorphic belt of Southeast Tibet. *International Journal of Earth Sciences*, 106(3), 875–897.

Xu, Z., Wang, Q., Cai, Z., Dong, H., Li, H., Chen, X., et al. (2015). Kinematics of the Tengchong Terrane in SE Tibet from the late Eocene to early Miocene: Insights from coeval mid-crustal detachments and strike-slip shear zones. *Tectonophysics*, 665, 127–148. https://doi.org/ 10.1016/j.tecto.2015.09.033

Zhang, B., Chai, Z., Yin, C. Y., Huang, W. T., Wang, Y., Zhang, J. J., et al. (2017). Intra-continental transpression and gneiss doming in an obliquely convergent regime in SE Asia. *Journal of Structural Geology*, 97, 48-70.

Zhang, B., Zhang, J., Liu, J., Wang, Y., Yin, C., Guo, L., et al. (2014). The Xuelongshan high strain zone: Cenozoic structural evolution and implications for fault linkages and deformation along the Ailao Shan–Red River shear zone. *Journal of Structural Geology*, 69, 209–233. https://doi.org/10.1016/j.jsg.2014.10.008

Zhang, B., Zhang, J. J., Zhong, D. L., Yang, L. K., Yue, Y. H., & Yan, S. Y. (2012). Polystage deformation of the Gaoligong metamorphic zone: structures, 40Ar/39Ar mica ages, and tectonic implications. *Journal of Structural Geology*, 37, 1-18.

Zhang, L. S., & Schärer, U. (1999). Age and origin of magmatism along the Cenozoic Red River shear belt, China. *Contributions to Mineralogy and Petrology*, 134(1), 67–85. https://doi.org/10.1007/s004100050469

Zhou, Y., Zhou, P., Wu, S. M., Shi, X. B., & Zhang, J. J. (2002). Magnetic fabric study across the Ailao Shan–Red River shear zone. *Tectonophysics*, 346(3-4), 137–150. https://doi.org/10.1016/S0040-1951(01)00269-4

Supporting Information References

Cao, S. Y., Neubauer, F., Liu, J. L., Genser, J., & Leiss, B. (2011b). Exhumation of the Diancang Shan metamorphic complex along the Ailao Shan-Red River belt, southwestern Yunnan, China: Evidence from 40Ar/39Ar thermochronology. Journal of Asian Earth Sciences, 42, 525-550.

Chen, X. Y., Liu, J. L., Qi, Y. C, Fan, W. K., Wang, K., Zhang, Y., & Chen, W. (2017a). Miocene structural evolution and exhumation of the Ximeng dome in Yunnan, southeastern Tibet: Implications for intraplate deformation during extrusion of the Sundaland block. Journal of Asian Earth Sciences, 141, 194-212.

Chen, X. Y., Liu, J. L., Weng, S. T., Kong, Y. L., Wu, W. B., Zhang, L. S., & Li, H. Y. (2016). Structural geometry and kinematics of the Ailao Shan shear zone: Insights from integrated structural, microstructural, and fabric studies of the Yao Shan complex, Yunnan, Southwest China. International Geology Review, 58(7), 849–873.

Chen, X. Y., Liu, J. L., Tang, Y., Song, Z. J., & Cao, S. Y. (2015). Contrasting exhumation histories along a crustal-scale strike-slip fault zone: The Eocene to Miocene Ailao Shan-Red River shear zone in southeastern Tibet. Journal of Asian Earth Sciences, 114, 174–187. https://doi.org/10.1016/j.jseaes.2015.05.020

Harrison, T. M., Leloup, P. H., Ryerson, F. J., Tapponnier, P., Lacassin, R., & Wenji, C. (1996). Diachronous initiation of transtension along the Ailao Shan–Red River shear zone, Yunnan and Vietnam, in Yin, A., and Harrison, T. M., eds., The tectonic evolution of Asia: New York, Cambridge University Press, 205–226.

Ji, J. Q., Zhong, D. L., Sang, H. Q., Qiu, J., & Hu, S. L. (2000). Dating of two metamorphic events on the basalt granulite from the Nabang area on the border of China and Burma. Acta Geologica Sinica, 16, 227e232.

Leloup, P. H., Arnaud, N., Lacassin, R., Kienast, J. R., Harrison, T. M., Trong, T. T. P., et al. (2001). New constraints on the structure, thermochronology and timing of the Ailao Shan–Red River shear zone, SE Asia. Journal of Geophysical Research, 106(B4), 6683–6732. https://doi.org/10.1029/2000JB900322

Leloup, P. H., & Kienast, J. R. (1993). High-temperature metamorphism in a major strike-slip shear zone: The Ailao Shan–Red River, People's Republic of China. Earth and Planetary Science Letters, 118(1-4), 213–234.

Li, B. L., Wang, D. D., & J, J. Q. (2014). Structure, Timing, and Mechanism of the Pliocene and Late Miocene Uplift Process of the Ailao Shan-Diancang Shan, SE Tibet, China. Acta Geologica Sinica (English Edition), 88, 1084–1101.

Li, B. L., Ji, J. Q., Fu, X. Y., Gong, J. F., Song, B., Qing, J. C., et al. (2009). Metamorphic time limits' study on the metamorphic rocks series of Ailao Shan Diancang Mountain Ranges, west Yunnan. Acta Petrologica Sinica, 3, 595–608 (in Chinese with English abstract).

Li, Q., Chen, W. J., Wan, J. L., & Li, D. M. (2001). New evidence of tectonic uplift and transform movement style along Ailao Shan-Re River shear zone. Science China, 44, 124–132.

Lin, T. H., Chung, S. L., Hsu, F. J., Yeh, M. W., Lee, T. Y., Ji, J. Q., et al. (2009). 40Ar/39Ar dating of the Jiali and Gaoligong shear zones: implications for crustal deformation around the Eastern Himalayan Syntaxis. Journal of Asian Earth Science, 34, 674-685.

Maluski H, Claude Lepvrier L, Jolivet A, et al. Ar-Ar and fission-track ages in the Song Chay Massif: Early Triassic and Cenozoic tectonics in northern Vietnam. Journal of Asian Earth Sciences, 2001, 19(1-2): 233-248

Wan, J. L., Li, Q., & Chen, W. J. (1997). Fission track evidence of diachronic uplift along the Ailao Shan-Red River left-lateral strike-slip shear zone. Seismology Geology, 19, 87–90 (in Chinese with English abstract).

Wang, G., Wan, J. L., Wang, E. Q., Zheng, D. W., & Li, F. (2008). Late Cenozoic to recent transtensional deformation across the Southern part of the Gaoligong shear zone between the Indian plate and SE margin of the Tibetan plateau and its tectonic origin. Tectonophysics, 460, 1-20.

Viola, G., & Anczkiewicz, R. (2008). Exhumation history of the Red River shear zone in northern Vietnam: New insights from zircon and apatite fission-track analysis. Journal of Asian Earth Sciences, 33, 78–90

Wang, D. D., Li, B. L., Ji, J. Q., Song, S. G., Wei, C. J., & Gong, J. F. (2013). The thermal evolution and deformation time limit of the Gaoligong metamorphic belt in western Yunnan. Acta Geologica Sinica, 87, 1887-1900.

Wang, Y. J., Fan, W. M., Zhang, Y. H., Peng, T. P., Chen, X. Y., & Xu, Y. G. (2006). Kinematics and 40Ar/39Ar geochronology of the Gaoligong and Chongshan shear systems, western Yunnan, China: implications for early Oligocene tectonic extrusion of SE Asia. Tectonophysics, 418, 235-254.

Zhang, B., Chai, Z., Yin, C. Y., Huang, W. T., Wang, Y., Zhang, J. J., et al. (2017). Intra-continental transpression and gneiss doming in an obliquely convergent regime in SE Asia. Journal of Structural Geology, 97, 48-70.

Zhang, B., Yin, C. Y., Zhang, J. J., Wang, J. M., Zhong, D. L., Wang, Y., et al. (2017). Midcrustal shearing and doming in a Cenozoic compressive setting along the Ailao Shan-Red River shear zone, Geochemistry Geophysics Geosystem, 18, 400–433, doi:10.1002/ 2016GC006520.

Zhang, B., Zhang, J. J., Zhong, D. L., Yang, L. K., Yue, Y. H., & Yan, S. Y. (2012). Polystage deformation of the Gaoligong metamorphic zone: structures, 40Ar/39Ar mica ages, and tectonic implications. Journal of Structural Geology, 37, 1-18.